

The Metal Content of Dwarf Starburst Winds: Results from Chandra Observations of NGC 1569¹

Crystal L. Martin^{2,3}

Caltech

Mail stop 105-24, Pasadena CA 91125

clm@astro.caltech.edu

Henry A. Kobulnicky

Astronomy Department, University of Wisconsin - Madison

475 N. Charter St., Madison, WI 53706

chip@astro.wisc.edu

Timothy M. Heckman

The Johns Hopkins University

Department of Physics & Astronomy

Baltimore, MD, 21218

ABSTRACT

We present deep, Chandra spectral imaging of the dwarf starburst galaxy NGC 1569. The unprecedented spatial resolution allows us to spatially identify the components of the integrated X-ray spectrum. Fitted spectral models require an intrinsic absorption component and higher metal abundances than previous studies indicated. Our results provide the first direct evidence for metal-enriched winds from dwarf starburst galaxies.

¹Based on observations obtained with the Chandra X-ray Observatory

²Also Physics Department, University of California Santa Barbara

³Visiting astronomer National Optical Astronomy Observatory (NOAO). NOAO is operated by the Association of Universities for Research in Astronomy (AURA), Inc. under cooperative agreement with the National Science Foundation.

We identify 14 X-ray point sources in NGC 1569. Most have properties consistent with those of high mass X-ray binaries, but one is a steep-spectrum radio source which is probably a supernova remnant. The X-ray luminosity of NGC 1569 is dominated by diffuse, thermal emission from the disk (0.7 keV) and bipolar halo (0.3 keV). Photoelectric absorption from the inclined HI disk hardens the X-ray spectrum on the northern side of the disk relative to the southern side. Requiring the fitted absorption column to match the HI column measured at 21-cm implies that the metallicity of the HI disk is significantly less than solar but greater than $0.1 Z_{\odot}$. Hence, much of the HI is enriched to levels comparable to the metallicity of the HII regions ($O/H = 0.2 (O/H)_{\odot}$). The X-ray color variations in the halo are inconsistent with a free-streaming wind and probably reveal the location of shocks created by the interaction of the wind with a gaseous halo. The X-ray spectrum of the diffuse gas presents strong emission lines from alpha-process elements. Fitted models require alpha element abundances greater than $0.25 Z_{\alpha, \odot}$ and ratios of alpha elements to iron 2 to 4 times higher than the solar ratio. The best fit to the spectrum is obtained with solar mass fractions for the alpha elements, $1.0 Z_{\alpha, \odot}$; but a degeneracy between the metallicity and the spectral normalization prevents us from deriving an upper limit on the wind metallicity from the X-ray spectrum alone. We argue, however, that abundances larger than $2.0 Z_{\alpha, \odot}$ pose awkward implications for the dynamical evolution of the wind based on our knowledge of the starburst properties. For consistency with our best fitting abundances, the mass of interstellar gas entrained in the wind must be about nine times the mass of stellar ejecta in the wind. Most of the oxygen carried by the wind comes from the stellar ejecta, rather than entrained interstellar gas. The estimated mass of oxygen in the hot wind, $34,000 M_{\odot}$, is similar to the oxygen yield of the current starburst. *Apparently the wind carries nearly all the metals ejected by the starburst.* These metals appear destined to contribute to the enrichment of the intergalactic medium. Much of the nucleosynthesis in NGC 1569 must have occurred during less violent periods of star formation, however, because our measurements imply the neutral gas disk holds at least five times more oxygen than wind.

Subject headings: galaxies: formation — galaxies: evolution — galaxies: fundamental parameters — galaxies: abundances

1. Introduction

Galactic winds have been advocated as a mechanism which disperses metals throughout galactic disks and the intergalactic medium (IGM). This paper presents new Chandra observations of the dwarf galaxy NGC 1569 which demonstrate that much of the metal-rich ejecta produced in the current starburst must reside in the hot X-ray wind. This result is of particular interest because the hot gas is not gravitationally bound to this intermediate mass dwarf galaxy (e.g., Heckman et al. 1995; Martin 1999).

1.1. NGC 1569

The nearby dwarf galaxy NGC 1569 entered a starburst phase 10 to 20 Myr ago (Israel & deBruyn 1988; Gonzalez-Delgado et al. 1997; Hunter et al. 2000). An encounter with a low-mass cloud of HI ($7 \times 10^6 M_\odot$ and 5 kpc away) in the IC 342 Group may have triggered the current activity (Stil & Israel 1998). The nearest galaxy with similar radial velocity, UGCA 92, lies at a projected distance of 60 kpc (Karachentsev, Tikhonov, & Sazonova 1994). The young stellar population spreads across the disk, which is inclined 60° to our sightline (Israel 1998), but is concentrated in the center where several super star clusters are found (O'Connell et al. 1994; Hunter et al. 2000). The two brightest clusters alone have probably produced several thousand supernovae, and the total starburst $\sim 30,000$. The energy imparted to the interstellar medium by these supernova explosions drives a bipolar outflow seen extending to either side of the disk in H α emission (Heckman et al. 1995; Martin 1998).

The coronal gas in the outflow was imaged in soft X-rays with ROSAT (Heckman et al. 1995), and ASCA spectra confirmed the emission mechanism was thermal (Della Ceca et al. 1996). The fitted ASCA temperature, 0.6 keV for MEKAL models or 0.8 keV for Raymond-Smith models (Della Ceca et al. 1996), was shown to be several times higher than the escape temperature from the dark matter halo (Martin 1999). Since the cooling time of the hot gas, about 100 Myr, is longer than the dynamical age of the outflow, about 10 Myr, the X-ray emitting gas appears likely to escape (e.g., Heckman et al. 1995). In order for the wind to stall, it must either encounter a very large mass of halo gas or undergo extensive mixing with cooler gas which would accelerate the radiative losses.

If this wind carries the bulk of the metals expelled by supernovae in the starburst population, it could solve a longstanding puzzle. The HII regions in NGC 1569 show no local enhancements of O, N, or He as would be expected if the material ejected from massive stars was mixed directly into the HII regions (Kobulnicky & Skillman 1997). This lack

of enrichment is most conspicuous in low metallicity galaxies (i.e., large dZ/Z) where it is common (Tenorio-Tagle 1996; Martin 1996; Kobulnicky & Skillman 1997). The galaxy NGC 1569 is particularly valuable as a case-study because of its proximity ($d = 2.2$ Mpc, Israel 1988), low escape velocity ($80\text{--}110 \text{ km s}^{-1}$, Martin 1999), and low metallicity ($0.20 \text{ (O/H)}_{\odot}$, Kobulnicky & Skillman 1997; Martin 1997). It is caught in a starburst phase, but otherwise is a typical dwarf with dynamical mass $M_{dyn} \sim 2 \times 10^8 \text{ M}_{\odot}$ (e.g., Martin 1998) and $L_{Bol} \approx 1.7 \times 10^9 \text{ L}_{\odot}$ (Israel 1988).

1.2. Abundance Determinations from X-Ray Spectra

In principle, abundance determinations for a collisionally-ionized plasma are easier than in the nebular case where photoionization must be included in the model. Under coronal conditions, the ionization structure is completely determined by the electron temperature which is fixed by external processes, the hydrodynamic shocks in the case of galactic winds. Metal abundances derived from thermal X-ray spectra have a controversial history, however, due to uncertainties in the atomic physics, different definitions of the solar abundance, and a number of degeneracies inherent to multi-component spectral models.

Reports of very sub-solar abundances in elliptical galaxies, for example, were met with skepticism, and have been traced in part to uncertainties in the Fe-L shell atomic physics (Liedahl et al. 1995). A degeneracy between high metallicity, two-temperature models and low metallicity, single-temperature models has also produced reports of surprisingly low metallicities (Buote & Canizares 1994). In spectra of galaxy clusters, relative abundances have proven difficult to constrain owing to blends between Fe-L lines and lines from alpha-process elements (Mushotzsky et al. 1996). Hence, the metallicities tend to be pushed lower than their true value if the temperature range is not fully represented. Weaver et al. (2000), see also Dahlem et al. 1998, have argued that supersolar $[\alpha/Fe]$ ratios in NGC 253 and M82 are ramifications of underestimating the absorbing column. Intrinsic absorption omitted from the spectral model will increases the apparent strength of Mg and Si lines relative to Fe-L lines. Unless lower energy lines from O are detected, a statistically acceptable fit can be obtained with an anomalously high alpha element to Fe abundance ratio. In spite of these common traps, we will argue that analysis of the Chandra data yield (1) a unique alpha to iron abundance ratio and (2) significantly constrain the absolute abundance of the outflow.

We adopt the MEKAL models implemented in XSPEC 10 (Arnaud 1996) which include the Fe L-shell calculations of Liedahl et al. (1995). They have been shown to provide accurate temperatures for elliptical galaxies with $kT = 0.7$ to 1.0 keV (Buote & Fabian 1997) and galaxy clusters (Mushotzsky et al. 1996). Since the line emissivity increases relative to the

continuum as the plasma temperature decreases from a few keV to a few tenths of a keV (e.g., Raymond & Smith 1977), it is somewhat easier to compare the alpha-element line strengths to the Fe-L lines in spectra of starburst galaxies which have cooler spectra. At temperatures ~ 0.5 keV, we find that relatively small, $\geq 10\%$, changes in metal abundance produce significant variations in the count distribution at the spectral resolution of the back illuminated Chandra CCD's (~ 100 eV).

In §2, we describe the Chandra observations and optical and radio observations. The latter define the amount and location of cooler gas as well as the geometry of the system – information that proves essential for breaking the spectral degeneracies. In §3, we use the spectral imaging capabilities of Chandra to isolate X-ray emission and absorption components. The integrated spectrum proves to be so complex, that this approach is the only way to build a physical model that breaks the various degeneracies summarized above. In §4, we derive the chemical properties of the X-ray emitting gas which are then improved upon when the dynamics of the outflow are considered jointly in §5. The main conclusions are summarized in §6 and have important implications for the chemical evolution of dwarf galaxies, the dynamics of winds, and the pollution of the IGM.

2. Data Acquisition and Reduction

2.1. Chandra Observations

The *Chandra* X-ray Observatory observed NGC 1569 with the AXAF CCD Imaging Spectrometer (ACIS) on 2000 April 11 for 96.8 ksec. The galaxy was placed on the back-illuminated chip ACIS-S3 (also known as chip 7). These data as well as the fields on the ACIS-I and ACIS-S5 chips are available in the archive under sequence number 600085.

The data were processed by the Chandra X-Ray Center (CXC) using version R4CU5UPD13.1 of their software. We checked the positional accuracy of the chip 7 Chandra sources using our R-band image (Section 2.2) and 20 cm radio map (Section 2.3). For the 16 X-ray sources with optical detections and 3 X-ray sources with radio counterparts, the maximum positional discrepancy was found to be $0.5''$. Reprocessing with CIAO version 2.1.3 was required to make the gainfile consistent with the revisions of 2001 August to the ACIS-S3 FEFs (for focal plane temperature of -120 C). The shifted energy scale and decreased spectral resolution, significantly improved the fit statistics of our best models. Periods of high background were defined by time intervals with count rates differing by more than a factor of 1.2 from the mean quiescent background rate on chip 7, i.e., 1.55 cnts/s. Eliminating these flares improved the signal-to-noise ratio of the data and reduced the net exposure time to 84.89

ksec.

2.1.1. Spectral Extraction

Spectra were extracted using pulse invariant data values to account for gain variations between nodes. For each source region, we weighted the appropriate CXC spectral response files by the distribution of their areas within the aperture.⁴ The maximum difference between our area-weighted response files and single response files extracted at the flux-weighted centroid of the aperture was a few percent. Weighting the response files by the distribution of counts within the aperture produced results indistinguishable from the area-weighted responses.

A background events file was constructed from deep ACIS observations of blank fields using software provided by M. Markevitch through the CXC. After normalizing to the net exposure time of the NGC 1569 observations, the source free regions of our data exhibit a count rate $\sim 4\%$ higher than the same regions in the blank-field background map. This discrepancy is consistent with the known slow, temporal decrease in the ACIS-S3 background rate described by Markevitch. After correcting the blank-field background rates by this factor of 1.04, we estimate the mean background rate is good to $\pm 1\%$ across the entire field.

2.1.2. Image Extraction

Unbinned images were extracted from the time-filtered events file in four carefully chosen bands: Soft (S) 0.3 – 0.7 keV, Medium (M) 0.7 – 1.1 keV, Hard (H) 1.1 – 6 keV, and total 0.3 – 6 keV. Emission in the soft band is highly attenuated because the Galactic foreground column, $N_H = 2.1 \times 10^{21} \text{ cm}^{-2}$ (Burton 1985), presents optical depth unity at 0.7 keV and $\tau = 6.5$ at 0.3 keV. The galaxy was not detected at energies above 6 keV, the energy adopted for the Hard band cutoff. Background images were extracted from the background events file, described above, in these bands.

Each of the four X-ray images was smoothed using the adaptive smoothing algorithm of H. Ebeling & V. Rangarajan as implemented in CSMOOTH (CIAO 2.0). The smoothing scales are automatically adjusted to achieve a minimum S/N ratio of 2 and a maximum S/N ratio of 3 per pixel. Strong point sources are effectively unchanged by the smoothing process,

⁴We used the `calcrmf/calcarf` software package contributed by Jonathon McDowell which is available from the CXC website – <http://asc.harvard.edu/cgi-gen/cont-soft/soft-list.cgi>.

while the contrast of weak, diffuse emission is enhanced. Each of the four background images was smoothed in the same manner and subtracted from the source images.

Since adaptive smoothing does not preserve photon statistics in a straightforward manner, we used the adaptively smoothed images only to produce images for presentation and to define apertures for the extraction of spectra. All quantitative analyses was performed by extracting photons from the events file or unsmoothed images and estimating their significance using Poisson statistics.

2.1.3. *Source Identification*

The CIAO 2.0 point source detection routine *celldetect* was run on the (unsmoothed) broadband 0.3-6 keV image to identify point-like sources. Visual examination of the resulting detections showed that some sources with a significance level as low as 1.9σ in the central portion of the chip corresponded to R-band sources (i.e., stars or background AGN). After several iterations of X-ray detection, image inspection, and optical counterpart searching, we adopted the following approach. In the central $1'$ of the S3 chip where the Chandra PSF is best, we set a minimum detection threshold of 1.9σ . For a 100 ks exposure, this threshold should lead to less than 1 false detection.⁵ For the region between 1 and $2.5'$ from the center of the chip, a detection threshold of 2.1 was used to achieve the same probable false detection rate. For the section of the chip beyond $2.5'$ from the center, we used a detection threshold of 3.2σ . The point spread function degrades significantly beyond $3.5'$, so we did not attempt to find point sources beyond this radius.

In regions within the main body of NGC 1569 where the local background due to diffuse emission is high, point source detection becomes less robust. To restrict our source list to point-like emission regions, we retained only those detections with sizes (as defined by the radius encircling 0.8 of the total flux) less than 2 times the size of the nominal Chandra PSF (i.e., sources with source-size to PSF ratios less than 2.0). The resulting 45 point-like sources are listed in Table 1 with their J2000 positions, counts extracted from the unsmoothed images, and 1σ uncertainties estimated using Poisson statistics. To avoid neighboring sources, background annuli were defined manually around each aperture defined by *Celldetect*. Within NGC 1569, the point sources detected at the lowest significance level all have very hard colors (count rates are highest in the H band) which is consistent with the signature of an X-ray binary (or perhaps background AGN) seen behind an HI column

⁵See the Chandra *Detect 1.0* users guide Section 4.6 for approximate detection thresholds as a function of false detection rate.

of few $\times 10^{21} \text{ cm}^{-2}$ but inconsistent with soft, thermal sources. We therefore believe that we have successfully culled local maxima in the diffuse emission from the sample in Table 1. In §3.1 we discuss the identify of the point sources further.

2.2. Optical Observations

Narrowband, optical images were obtained at $\text{H}\alpha$ (6571 Å, 84 Å FWHM) and in the adjacent continuum (6487 Å, 67 Å FWHM) at the KPNO 2.1 m telescope 2000 January 2–10. Fixed pattern noise was removed from the CCD frames in the standard way using short bias level exposures, dome flats, and twilight sky flats. The scaled, continuum image was subtracted from the on-band image to produce an [NII]+ $\text{H}\alpha$ image. The images were flux calibrated using observations of spectrophotometric standard stars (Massey et al. 1988). The $\text{H}\alpha$ flux was corrected for [NII] 6548,84 emission using the luminosity-weighted value of the [NII] 6548,84/ $\text{H}\alpha$ flux ratio, 0.042 (Martin 1998). We measured the Balmer decrement along longslit spectra, previously described by Martin (1997), and estimate the luminosity-weighted average extinction is $A(\text{H}\alpha) = 1.48$ mag (for a ratio of general to selective extinction $R = 3.1$). The resulting extinction-corrected $\text{H}\alpha$ luminosity is $5.04 \times 10^{40} \text{ ergs s}^{-1}$.

In dust-poor galaxies, the $\text{H}\alpha$ luminosity provides an excellent measure of the star formation rate (SFR) (e.g., Kennicutt 1998 and references therein). It is directly proportional to the ionization rate and, hence, the number of stars with masses greater than about 20 M_\odot . For a stellar initial mass function (IMF) with power law index $\alpha = -2.35$ from 1.0 M_\odot to 100 M_\odot , the $\text{H}\alpha$ luminosity implies a SFR of $0.16 \text{ M}_\odot \text{ yr}^{-1}$ (Leitherer & Heckman 1995; Kennicutt 1998). The main uncertainty in the SFR is the variation in extinction among the HII regions and warm, diffuse ionized medium (Kobulnicky & Skillman 1997; Martin 1997). Ionizing radiation absorbed by dust will be re-radiated in the far infrared, however, so we can check the maximum magnitude of our error. The IRAS fluxes give a total L_{FIR} of $5.63 \times 10^8 \text{ L}_\odot$, which is about half of the B-band luminosity of $1.3 \times 10^9 \text{ L}_\odot$ (Israel 1988). Their sum L_{Bol} implies a SFR of $0.17 \text{ M}_\odot \text{ yr}^{-1}$ (Meurer et al. 1997). Since the optical and infrared estimates agree, dust obscuration does not significantly change the estimated SFR. (Note that the star formation rate would be 2.5 times higher if the IMF is extended from 1.0 M_\odot to 0.1 M_\odot .)

2.3. Radio Observations

We obtained VLA 3.6 cm (8 GHz) radio continuum observations from the VLA archive database. Approximately 65 minutes of data were originally obtained on 21 Aug 1990 in the B configuration using a bandwidth of 50 MHz. After standard phase and flux calibration in AIPS, we mapped the field of NGC 1569. The resulting maps have a beamsize of 1" and a 1σ RMS noise level of 0.03 mJy/beam. We detected 1 source projected on the disk of NGC 1569.

As part of a larger radio continuum study of NGC 1569, we obtained 20 cm (1.4 GHz) continuum observations of NGC 1569 for 3 hours on 13 May 2001 in the B configuration using a bandwidth of 50 MHz. After standard phase and flux calibration in AIPS, we mapped the field of NGC 1569. The resulting maps have a beamsize of 5" and a 1σ RMS noise level of 0.038 mJy/beam. Only 1 source was detected toward NGC 1569. A recent 20 cm study at higher resolution (Greve et al. (2002) finds two additional sources besides the VLA source. Including two marginal detections reported in the Greve et al. work brings the total number of radio SNR candidates to 5.

3. General Properties of the X-Ray Emission from NGC 1569

Previous observations with the High Resolution Imager on ROSAT show that half of the ~ 1 keV flux from NGC 1569 comes from a diffuse halo of dimensions $\sim 3.8' \times 2.2'$ (Heckman et al. 1995, Heckman et al. 1995). Spectral models fitted to ASCA observations (Tanaka, Inoue, & Holt 1994; Della Ceca et al. 1996) firmly establish the presence of a soft, thermal emission component which likely emanates from this extended emission (Della Ceca et al. 1996). In contrast, the nature of the harder, $kT = 3 - 4$ keV or $\Gamma \approx 2$, component has not been well constrained. The X-ray luminosity of the halo emission is too bright to come entirely from hot, supernovae ejecta; but entrainment of ambient, interstellar gas in the hot wind can easily boost the luminosity to the observed value (Heckman et al. 1995; Martin & Kennicutt 1996). The location and nature (i.e., evaporation or ablation) of this mass loading has not been established however. We exploit the spatial resolution of the Chandra observations to describe (and remove) the point source population, examine the relative morphology of the cold, warm, and hot gas, and relate these components to the integrated X-ray spectrum.

3.1. Point Sources

3.1.1. Sources Associated with NGC 1569

Figure 1 shows a region near the nucleus of NGC 1569 with identification numbers from Table 1 near each X-ray source. Fourteen point sources lie projected on the main stellar disk of NGC 1569 (numbers #14–19 and #22–29) and likely reside within NGC 1569. Figure 2 shows the strongest X-ray sources on the HST WFPC2 F555W image (courtesy of Deidre Hunter; Hunter et al. 2000). None of the X-ray sources coincide with the two most prominent optical features – super starclusters “A” and “B” (Arp & Sandage 1985). X-ray sources #19 and #22 do coincide with fainter starclusters designated #29 and #34, respectively, by Hunter et al. (2000). Table 1 includes these probable identifications along with the F555W magnitudes of the clusters from Hunter et al. (2000). The other 12 X-ray sources which lie projected against the main disk of NGC 1569 do not have obvious optical counterparts, and approximate upper limits are listed in Table 1 for their R-band magnitudes. Four X-ray sources were detected in the VLA radio observations, but only source #28 appears to be associated with NGC 1569. The MERLIN observations (Greve et al. 2002) detect our source #14 (M-3) as well #28 (M-6)

Source #28 has a radio spectral index, $\alpha_3^{20} = -0.9$. The steep spectrum suggest a non-thermal origin and is typical of evolved supernova remnants (Weiler & Sramek 1988). Optical line imaging in [OIII] $\lambda\lambda 5007, 4959$ and [SII] $\lambda\lambda 6717, 31$ reveals a small shell at this location confirming the identification as a supernova remnant which is particularly spectacular in the HST imaging presented by Shopbell et al. (2000). The 20 cm radio flux of 5.6 mJy implies a spectral luminosity of $3.2 \times 10^{25} \text{ erg s}^{-1} \text{ Hz}^{-1}$ which is approximately as luminous as Cas A, the most luminous SNR in the Milky Way at $3.5 \times 10^{25} \text{ erg s}^{-1} \text{ Hz}^{-1}$ and nearly as luminous as the ultra-luminous SNRs in M 82 ($3.2 \times 10^{25} \text{ erg s}^{-1} \text{ Hz}^{-1}$; Allen & Kronberg 1998). With 25 photons detected from 0.3–6 keV (0.0003 ph/s), the implied flux is $2.6 \times 10^{-15} \text{ erg s}^{-1} \text{ cm}^{-2}$ for a 0.2 keV blackbody and $N(H) = 8 \times 10^{21} \text{ cm}^{-2}$. The implied unabsorbed luminosity at 2.2 Mpc is $1.4 \times 10^{36} \text{ erg s}^{-1}$, comparable to the X-ray luminosities of SNR’s in NGC 300 (Pannuti et al. 2000) or M101 (Pence, Snowden & Mukai 2001).

Comparison of the brightest point sources detected with Chandra to the sources seen in the ROSAT HRI study of Heckman et al. (1995) reveals significant variability. Our Source #16 corresponds to Source #1 of Heckman et al. (1995) and is approximately 3 times more luminous in 2000 May Chandra data than in 1992 March ROSAT data. Source #2 of Heckman et al. (1995) has vanished, and it is not present in the 2000 Chandra data to the detection limit of $1.2 \times 10^{-16} \text{ erg s}^{-1} \text{ cm}^{-2}$. Two of the strongest sources in 2000 May, our #19 and #22, have apparently turned on since 1992 March, since they do not appear at all

in the ROSAT map. This variability is readily explained if the sources are accreting X-ray binaries.

To compare the properties of all 14 point sources projected against NGC 1569, we measured X-ray colors sensitive to absorbing column, $C_1 \equiv (M - S)/(M + S)$, and spectral hardness, $C_2 \equiv (H - M)/(H + M)$. The top panel of Figure 3 shows all the sources are harder than the supernova remnant, #28, so most are likely accretion powered binaries. Their location in the starburst region indicates they are high mass X-ray binaries. Indeed, since radio-bright SNRs are predicted to be older than the X-ray-bright remnants (Chevalier & Fransson 2001), a large number of X-ray SNRs would have been surprising in NGC 1569.

We extracted spectra of the brightest sources, #16 and #19. The fitted emission models, summarized in Table 2 rule out a blackbody emission model but do not distinguish between a thermal MEKAL model and a power law model. Adopting the power law model for consistency with the X-ray binary interpretation, the implied unabsorbed luminosity is $3.1 \times 10^{38} \text{ erg s}^{-1}$ for source #16 and $5.4 \times 10^{37} \text{ erg s}^{-1}$ for source #19. The estimated unabsorbed 0.3–6 keV luminosities for the other sources range from $1.2 \times 10^{35} \text{ erg s}^{-1}$ to $1 \times 10^{37} \text{ erg s}^{-1}$, where we have assumed a mean photon index of $\Gamma = 3.0$ and a total foreground column of $0.21 \times 10^{22} \text{ cm}^{-2}$ (see Figure 3).

The models in Figure 3 demonstrate that the point sources require foreground absorption columns of 0.6 to $1.6 \times 10^{22} \text{ cm}^{-2}$, *in addition to* the Galactic foreground of $N(\text{H}) = 0.21 \times 10^{22} \text{ cm}^{-2}$. Using a 21-cm map kindly provided by E. Wilcots (pvt. comm), we found the inferred X-ray absorption columns toward individual point sources are loosely correlated with the 21-cm intensity in the same direction. Most notable are the two brightest sources which lie in a previously described HI hole (Israel & van Driel 1990).

Figure 4 shows the cumulative luminosity function of the NGC 1569 point sources in the hard band (1.1–6 keV). With only 14 data points, we do not attempt to fit the slope. The solid line simply illustrates a typical power law index $\alpha = 0.5$, where $S(> C) = KC^{-\alpha}$, for the point source population in star-forming galaxies (Prestwich 2002; Tennant et al. 2001). We have normalized it to the highest luminosity bin which contains 5 sources with a total of 1400 counts in the 1.1–6.0 keV band. This luminosity function predicts a total of 1800 counts in the hard band, only 18% more than the observed total of ~ 1520 in the 14 identified point sources. If the slope of the luminosity function were steeper, say $\alpha = 0.9$, then the total predicted contribution from unresolved sources in the hard band would be 6300 counts, more than 4 times the total observed. However, this slope would predict 400 hard sources with more than 10 counts in the 85 ksec integration. Given that we have detected point sources to a completeness level of essentially 100% for sources > 10 counts, the fact that we only detect 9 sources with more than 10 counts in the hard band constrains the hard X-ray

luminosity function to values $\alpha \leq 0.55$. In conclusion, 1) the slope, α , of the cumulative hard X-ray luminosity function, is constrained to be $\alpha \sim 0.5$ and 2) the total hard counts from unresolved X-ray point sources do not contribute more than 18% above the contribution from the 14 currently-identified point sources. The diffuse emission can therefore be studied with little contamination from the point source population by filtering out the catalogued point sources.

3.1.2. Other Sources Projected Near NGC 1569

Of the 31 X-ray sources which lie outside of the main body of NGC 1569, about half coincide with point-like optical counterparts and are probably foreground Galactic stars. Others may be background AGN. We make tentative identifications by considering the ratios of X-ray to optical flux, f_X/f_V . Table 1 lists this ratio for each source. Based on Figures 2 and 3 of Krautter et al. (1999), we tentatively identify objects with $f_X/f_V > -0.5$ as stars, and objects with $f_X/f_V < -0.5$ as probable AGN. Using this criterion, 15 objects are probable AGN and 16 are stars. Given the 2σ sensitivity limit of $\sim 4 \times 10^{-16} \text{ erg}^{-1} \text{ cm}^{-2}$ in the broadband 0.3–6 keV image, we would expect 16 ± 4 extragalactic background sources over the $7' \times 7'$ area analyzed on the S3 chip, based on the Chandra Deep Field South count rates (Rosati et al. 2001). This is consistent with the 15 objects we have tentatively identified as background AGN.

The lower panel of Figure 3 shows the 31 sources which lie outside NGC 1569, coded by their identification as either Star or AGN. Lines denote MEKAL thermal plasmas with temperatures $kT=1.0$ keV and $kT=2.0$ keV for five different foreground HI column densities as labeled. Objects identified as probable stars in Table 1 on the basis of f_X/f_V occupy a broad locus with lower implied HI column density than the probable AGN which cluster more tightly and have higher implied foreground column density. This separation provides an independent way to separate probable foreground stars from extragalactic objects.

3.2. Spatially Extended X-Ray Emission

3.2.1. X-Ray Morphology

Figure 5 shows the X-ray surface brightness contours around NGC 1569. The halo emission consists of two pairs of lobes at position angle 50° (NE and SW lobes) and 160° (NW and SE lobes) which were previously detected in the ROSAT imaging (Heckman et al. 1995; Della Ceca et al. 1996). The signal-to-noise ratio in the northeast lobe, at a projected distance

of 1.682 kpc, is 5σ and 7σ in the soft and medium bands, respectively. The detection level of the southwest lobe, at 1.912 kpc, is 2σ . Two point sources (#30 and #31), not believed associated with the galaxy, contribute to the emission from the southeast lobe. In contrast to the halo contours, the higher surface brightness contours in Figure 5 lie within $40''$ of the major axis and follow the ellipticity of the optical disk. This change in the morphology of the contours suggests that at least two physical components of the galaxy contribute to the diffuse emission. It is also interesting to note that the intensity gradient is steepest toward the west edge of the disk where molecular clouds have been detected (e.g., Taylor et al. 1999). The shock that is heating the hot disk gas is likely encountering the densest regions of the disk there.

Heckman et al. (1995) and Della Ceca et al. (1996) previously noted that the position angle of the lobes matches that of the most extended $\text{H}\alpha$ emission. The nature of this correspondence can now be seen more clearly in Figure 5 and Figure 6 as well as in the color image of Figure 7. The northeast lobe is bounded by filaments 12 and 13 (names from Hunter et al. 1993). Filament 11 marks the western edge of the northwest lobe. The X-ray surface brightness falls off abruptly where the southwest lobe meets the bright $\text{H}\alpha$ *arm*, and Filament 10 marks the extent of the hot gas further above the disk plane. To the southeast, the intensity of the halo emission declines sharply beyond Filament 7, but Filament 8 follows the most extended emission. In Figure 7, much of the periphery of the X-ray nebula (green) is marked by faint $\text{H}\alpha$ filaments (red). Hence, the X-ray emission is detected over the full extent of the $\text{H}\alpha$ nebula but not convincingly beyond it.

The location of the cooler (i.e., $\text{H}\alpha$ emitting) gas is therefore consistent with a web of filaments surrounding the hot halo. In the NGC 253 superwind, the X-ray emission appears to come mainly from a boundary layer adjacent to the shell rather the entire interior of the bubble (Strickland et al. 2000). In contrast to the cone-like geometry of the NGC 253 wind, the hot halo gas in NGC 1569 emanates from nearly the entire disk and maintains roughly the same diameter to distances at least 2 kpc above the midplane of the disk, whose position is indicated by the 21 cm contours in Figure 7). Much of the disk plane is clearly filled with hot gas, and the X-ray lobes appear to fill a large fraction of a cylindrical volume of radius similar to that of the star-forming disk. The X-ray halo is believed to be limb brightened in the southwest arm but appears more diffuse in the other lobes.

The cavities of the bubbles are easier to identify kinematically, since the limbs of the shells show no Doppler shift. The location of local maxima in the line-of-sight expansion speed (measured from the $\text{H}\alpha$ emission) are marked by the letters (from Martin 1998) in Figure 6. Near the base of Shell A and Shell E, the X-ray contours poke outwards into the lobes at $\text{PA}=50^\circ$. The NW lobe also appears to fill the region defined kinematically by Shell B.

Somewhat brighter contours, about $30''$ from the midplane, protrude into the expanding cavities that define Shell D and Shell G. This correlation between the X-ray intensity and the kinematics of the warm gas suggests some of the X-ray emission comes from near the center of the bubbles. The exception is the strong intensity enhancement just inside the southwest arm which we attributed to boundary layer emission.

3.2.2. X-Ray Color

Figure 8 shows the composite color X-ray image obtained from our Soft (red), Medium (green), and Hard (blue) images. The spatio-spectral information immediately isolates the dominate spectral components. First, the hardest emission (blue) comes from the point sources which are concentrated toward the center of the disk. Second, a strong color gradient is visible across the galactic disk, perpendicular to the major axis. The emission is harder (more blue) north of the midplane. Third, in the southern halo, the ~ 1 keV emission (green) is prominent along the inner (i.e., concave) side of Filament 6, near Filaments 11 and 10, and around Filament 5. In contrast, the softest halo emission (red) is not correlated with bright $\text{H}\alpha$ features. The softest regions in the NE lobe are also well inside the $\text{H}\alpha$ filaments. The point sources were shown to be hard sources in a previous section, and in § 4.1 we show quantitatively that photoelectric absorption from the inclined gas disk produces the color gradient across the disk.

The surprising characteristic of Figure 8 is the color variation in the halo. The halo does not present a simple radial spectral softening as would be expected from a free flowing wind cooling adiabatically (e.g., Chevalier & Clegg 1985). The emission is strongest in the Medium band (green regions) near the bright $\text{H}\alpha$ filaments. The Soft band (red regions), in contrast, become more prominent between the filaments. The location of the softest regions in the X-ray color C_1 are denoted by the minima of the contours in Figure 9. The regions with the softest color, most visible in the southern halo, clearly emit the lowest total X-ray intensity. In contrast, the high surface brightness regions have a *green* color in Figure 8, emit most of the halo luminosity, and must be denser regions of the plasma. Any physical model must explain why the brighter, denser regions are located near the $\text{H}\alpha$ filaments.

To produce the observed X-ray luminosities, a wind must be confined by a dense shell of halo gas or loaded with entrained interstellar gas (e.g., Suchkov et al. 1996). A shocked shell could produce the observed limb brightening. Alternatively, the mixing layer of intermediate temperature gas between the shock and the wind fluid could generate most of X-ray emission. Unlike NGC 253, where all the halo emission in the Chandra observation is attributed to such mixing layers (Strickland et al. 2000), Figure 8 also reveals the lower surface brightness

wind fluid – i.e., the *redder* regions.

Our spectral fitting, see §3.3.3, constrains only the temperature of the bright, limb-brightened component. The soft emission is too faint for spectral analysis. We can compare the colors of these regions, however. The colors of the red regions are $C_1 = (M - S)/(M + S) = 0.36 \pm 0.07$ and $C_2 = (H - M)/(H + M) = -0.29 \pm 0.07$. The green region is harder in the soft color, $C_1 = 0.65 \pm 0.05$, but softer in the hard color, $C_2 = -0.41 \pm 0.06$. The bright halo regions (green) are harder than the faint (red) regions in the color $C_1 = (M - S)/(M + S)$, so they are likely more absorbed. Comparison to the colors of the equilibrium, thermal emission models in Figure 3b indicates the absorbing column could be as much as $1 \times 10^{21} \text{ cm}^{-2}$ higher toward the limb brightened regions. This amount of differential attenuation seems plausible based on the spatial variations shown in deep, 21 cm map of the halo (Mühle, 2002, pvt. commn.). Comparison of our C_1 color map in Figure 9 to her HI map on a point by point basis did not yield a simple correlation, but further investigation may clarify the relation of the C_1 to the absorption pattern.

The bright halo regions (green) are actually marginally softer than the *red* regions in the color C_2 . The red regions may include hotter gas. Alternatively, they could have a higher abundance of alpha elements relative to Fe. The Fe L emission lines contribute much of the flux in our Medium band, while strong lines from alpha-process elements are present in both the Soft band (OVII 0.574 keV, OVIII 0.653 keV) and Hard band (Mg XI 1.34, 1.35 keV, Si XIII 1.87 keV).

3.3. The Integrated Spectrum

Figure 10 shows the integrated X-ray spectrum.⁶ Absorption from the Galactic halo causes much of the soft energy turnover. We illustrate the contribution of the point sources previously identified § 2.1.3. Their contribution is clearly harder than the total spectrum and shows no emission lines. The remaining diffuse emission presents strong lines from OVII 0.57 keV, OVIII 0.65 keV, NeIX 0.905, 0.922, 0.915 keV, NeX 1.1016 keV, MgXI 1.34, 1.35 keV, and SiXIII 1.87 keV. The count rate peaks just below 1 keV where Fe L-shell lines, most prominently FeXVII, are blended at the energy resolution of the Chandra CCDs (a few hundred eV). Note that the line spectrum is not sensitive to the details of the background

⁶The integrated spectrum was extracted from an elliptical aperture enclosing the galaxy at 67.706143° , 64.844363° (J2000) with position angle 30° , major axis $322''$, and axis ratio of 0.582.

subtraction.⁷ The spurious feature at 1.6 keV in both the data and the background is thought to be an artifact of the gain tables.

The energy distribution of the counts from the diffuse emission is quite broad compared to the folded spectrum of any single-temperature thermal emission model. (See the fit statistic of the single-temperature model in Table 3!) By suppressing the emission lines, the fitting routine can increase the normalization which broadens the count distribution. When we allowed the metallicity to be driven to the unphysically low value of $0.06 Z_{\odot}$, the fit statistic was improved to $\chi_{\nu^2} = 1.55$, which is still unacceptable. We therefore conclude that the diffuse emission is inherently multi-temperature.

3.3.1. Comparison to Previous Spectral Models

Della-Ceca et al. (1996) excluded single-temperature thermal models on the same basis in their analysis of the joint ASCA and ROSAT/PSPC datasets for NGC 1569. They suggested two components, representing the disk and halo emission, are required and discussed four such models (RS+RS, M+M, RS+Po, and M+Po). The red curve in Figure 11 shows the residuals from their M+M model folded through the Chandra response. The Chandra data require a 17% higher normalization. The fit statistics in Table 3 do not distinguish the M+M and M+Po models. The MEKAL models fit slightly better than the Raymond-Smith models at low energy, and we use them for discussion in the rest of our analysis. The fitted temperatures are slightly higher for the Raymond-Smith models.

The residuals of the renormalized Della Ceca et al. (1996) M+M model are shown in the bottom panel of Figure 11. Della Ceca et al. (1996) attributed the residuals around 0.6-0.7 keV (near the oxygen lines) to calibration problems. Although the calibration of the Chandra response below ~ 0.7 keV is not firmly established, the reappearance of the residuals in data from a different observatory suggests they are real. More importantly though, the Della Ceca et al. (1996) M+M model fails to reproduce the strong Mg XI lines seen in the spectrum at ~ 1.3 keV. The residuals near the NeIX and NeX complex are also significant. Taken together, these shortcomings indicate the line emission of the model is too weak. We can use the spatial information afforded by the Chandra data to construct a better model of the spectrum.

⁷We use the background extracted from the data at large radii, and corrected for effective area. The background in the data has a slightly higher normalization at low energy, $E < 0.55$ keV, than that obtained from the simulated background. The difference, a factor of 1.7, is consistent with the spectral variability among pointings in the data sets used for the background simulation (Markevitch, pvt. comm.).

For consistency with previous analyses of ROSAT and ASCA observations of NGC 1569 (Heckman et al. 1995; Della Ceca et al. 1996), we adopt $N_{\text{H,Gal}} = 2.1 \times 10^{21} \text{ cm}^{-2}$; but the foreground column could be up to 20% lower. The galaxy is projected only 11° above the Galactic plane. Measurement of the Galactic N_{H} column is complicated by the proximity of emission from NGC 1569 in velocity space ($v_{\text{sys}} = -77 \text{ km s}^{-1}$ and 119 km s^{-1} FWZP, Reakes 1980). Averaged over a scale of $30'$, the total HI column toward NGC 1569 is $2.1 \times 10^{21} \text{ cm}^{-2}$ (Burton 1985). However, the average of eight profiles extracted $30'$ away from NGC 1569 gives a foreground column of $N_{\text{H,Gal}} = (1.93 \pm 0.16) \times 10^{21} \text{ cm}^{-2}$.⁸

3.3.2. Revised Spectral Components

The strong X-ray color variations described above led us to suspect that the absorbing columns of the two spectral components were different. Figure 11 shows another model (blue line) in which the intrinsic absorption of each thermal component was allowed to vary independently. It fits the count distribution around MgXI better as shown by the residuals in the bottom panel and the fit statistics in Table 3. The harder, 0.7 keV, component is several times more absorbed than the soft, 0.3 keV, component. In this model, the Mg line becomes stronger (and better describes the data) because the extra absorption allows for a lower temperature for the hard component than Della Ceca et al. derived. Both thermal components contribute significantly to the Mg line emission in our revised model.

We introduce a third emission component to describe the contribution of the X-ray point sources to the integrated spectrum. We fitted the summed spectra of the point sources, blue line in Figure 10, with a single power law model since it shows no prominent line emission. The point source population is adequately described by an absorbing column of $N_{\text{H}} = 2.3 \times 10^{21} \text{ cm}^{-2}$, power law index $\Gamma = 2.40$, and normalization of 8.40×10^{-5} photons $\text{keV}^{-1} \text{ cm}^{-2} \text{ s}^{-1}$ (at 1 kev). (This absorption is in addition to the foreground column of $2.1 \times 10^{21} \text{ cm}^{-2}$ and has an assumed metallicity of $0.25 Z_{\odot}$). Since the normalization of the power law component is quite low, a description of the integrated spectrum still requires two components to produce the wide spread in energy exhibited by the counts as shown by the final model in Table 3.

In summary, in contrast to Della Ceca et al. (1996), we find strong evidence for absorption intrinsic to NGC 1569. Including this intrinsic absorption in the spectral model drives

⁸The 21-cm $T_A(v)$ profile toward NGC 1569 shows five local maxima between -150 km s^{-1} and 30 km s^{-1} . If only the emission at $v < 30 \text{ km s}^{-1}$ was attributed to the foreground component, the absorbing column is reduced to $N_{\text{H,Gal}} = 1.7 \times 10^{21} \text{ cm}^{-2}$.]

the temperatures fitted to the two thermal components lower. The fraction of the flux coming from point sources increases toward higher energies. In our Hard band, point sources contributes 57% of 1.1 to 6 keV flux. The thermal components emit strong lines (e.g., MgXI 1.343, 1.352 keV and SiXIII 1.87 keV) in the Hard band. The 0.25 keV thermal component emits 72% of the Soft band flux. The total 0.3–6 keV flux is 4.11×10^{-13} erg s^{−1} cm^{−2}, and the unabsorbed luminosity in this band is 1.02×10^{30} ergs s^{−1}.

The shortcomings of this *wabs*pow + wabs*mek + wabs*mek* description are the remaining line residuals, most noticeably around MgXI. One way to boost the MgXI line is to add a third thermal component with a high normalization and a high intrinsic absorption component. Columns of order $N_H \sim 10^{22}$ cm^{−2} would be required, however, to avoid overproducing the OVII and OVIII line emission. This solution seems unlikely because the galaxy contains no known gas component that would cause such extreme absorption in the halo. Such high columns, if present, would have to be confined to small regions unresolved by the 21 cm observations; but the MgXI line emission seems to come from a large area. To find acceptable fits to the lines, we vary the element abundances as described in §4.2.

3.3.3. Fits to Southern Halo Spectrum

To better understand the composite nature of the southern outflow, we extracted spectra from the *red* and *green* regions in Figure 8 separately. (Recall that the green regions have higher X-ray surface brightness and are found adjacent to the brightest H α filaments to the south of the disk, while the red regions are spatially correlated with the centers of the bubbles.) The count distributions in Figure 12 illustrate the deficit of 0.7 to 1.1 keV counts in the *red* regions relative to the *green* regions. A MEKAL model with photoelectric absorption provides an excellent description of the *green* regions. The best fit parameters are $kT = 0.30$ keV, $N_H = 3.4 \times 10^{21}$ cm^{−2}, and $norm = 8.9 \times 10^{-5}$ cm^{−5}. The reduced chi-squared value is 0.93, and the iron group abundance is 0.48 when the alpha elements are fixed at solar abundance. The bright regions in the southern halo with the *green* color are clearly the origin of the soft, 0.3 keV, component in the integrated spectrum.

The poor quality of the *red* spectrum (about 400 counts) does not allow us to distinguish between a model of a hotter plasma with minimal absorption and one with a very high alpha element to iron abundance ratio. However, for purposes of illustration, we extracted a spectrum of the diffuse emission south of the galactic midplane (apertures S1-5) and fitted a two temperature model. Table 4 summarizes the results. Like our model for the integrated spectrum, models of the emission from the southern half of the galaxy also require two thermal components. The only change to the 0.7 keV component is a decrease in the

normalization which is consistent with removing half of the volume from the aperture. The fitted absorbing column for 0.3 keV component is also significantly lower, which probably reflects the relative geometry of the two lobes. These results support the physical association of the hotter thermal component with the flow in the disk and the cooler one with the halo. The second halo component is too weak to affect the integrated spectrum much.

4. X-Ray Measurements of Metallicity

Each component added to the model of the integrated spectrum was spatially identified in the spectral-imaging data. Such spectral decomposition is a necessary prerequisite for fitting abundances. Otherwise, several degeneracies (e.g., between metallicity and temperature, emission measure, and absorbing column) can lead to unphysical, yet statistically acceptable, solutions for the abundances.

Before using our spectral model to investigate the metallicity of the hot wind, we examine one of the new spectral components – the disk absorption – in more detail. Since the photoelectric absorption cross section is dominated by metals at energies greater than 0.25 keV (Morrison & McCammon 1983), the equivalent hydrogen column is sensitive to the assumed metal abundance of the disk gas. We fit the X-ray absorption column and compare it to optical and radio measurements of the H column to constrain the metallicity of the gas disk.

4.1. Disk Absorption and Metallicity

Figure 13 shows the relevant geometry of the disk and wind. North (south) of the major axis, the gas kinematics indicate the wind is pointed away from (toward) our sightline (Israel & van Driel 1990; Heckman et al. 1995; Martin 1999). The prominent change in X-ray color perpendicular to the major axis of the disk, i.e., the emission is harder on the north side of the midplane, is consistent with the northern lobe of the outflow being viewed through the disk because lower energy X-rays are most easily absorbed.

To measure the projected gradient in the absorbing column, we assumed that SSC A is near the dynamical center of the disk (Israel & van Driel 1990; Stil & Israel 1999) and extracted spectra at 20'' (213 pc) intervals along the minor axis as illustrated in Figure 6. Figure 14 shows the deficit of soft counts in the northern spectrum relative to the southern spectrum for several pairs of apertures. For comparison, the spectra are normalized at high energies since the summed northern spectrum (N1-5) has $\sim 50\%$ fewer counts than the

summed southern spectrum (S1-5). For a solar metallicity disk, the N1-5 spectrum requires an additional absorbing column of, $\Delta N_H \approx 1.6 \times 10^{21} \text{ cm}^{-2}$ relative to the column toward S1-5 spectrum. Comparison to the S1 and N1 spectra in Figure 14 indicates that this difference comes largely from emission at projected heights of 0 to 20" (aperture 1).

We also fitted spectra from apertures S1, N1 and N2, which are marked in Figure 6, individually. A thermal emission model (MEKAL, $0.25 Z_\odot$) with variable photoelectric absorption and a fixed Galactic column (solar metallicity) was used in each case. Figure 15 shows the variation in absorbing column with projected height above the disk for three different values of the disk metallicity. To the north, the fitted absorbing column drops with projected distance from the midplane. The gradient is measured out to a projected midplane distance of 40" in absorption, which corresponds to galactocentric radii of ~ 426 pc. South of the disk midplane, the fitted column at point S1 is lower than that at N1 but does not drop all the way to the foreground value. The scale height of the absorbing gas must be $\gtrsim 123$ pc to produce this absorbing column south of the midplane.

The projected N(HI) column measured in 21-cm emission (Israel & van Driel 1998) shows a similar gradient as illustrated by the solid black line in Figure 15. The equivalent hydrogen columns inferred for the solar metallicity disk model are all significantly lower than the HI emission column. To match the measured hydrogen column, the disk metallicity must be less than solar. The green points in Figure 15 show that reducing the disk metallicity to $0.25 Z_\odot$ produces fitted X-ray absorption columns consistent with the 21-cm emission data. If the disk metallicity is further reduced to $0.1 Z_\odot$, the inferred X-ray column is inconsistent with the 21-cm HI column.

Absorption from metals in the warm, ionized disk could drive the fitted metallicity lower (shifts the black curve further to the right in Figure 15). We therefore estimated the intrinsic and foreground ionized gas columns from their H α emission measure. For a volume filling factor of 1%, the average column toward the H α nebula ($R = 2$ kpc) is $2.8 \times 10^{19} (\epsilon/0.01)^{0.5} \text{ cm}^{-2}$. The foreground Galactic column estimated from WHAM data assuming a pathlength of 1 kpc is $(3 - 6) \times 10^{19} (\epsilon/0.01)^{0.5} \text{ cm}^{-2}$ (Reynolds et al. 1998). Both of these values are small compared to the HI columns. We therefore conclude that the mean metallicity of the disk gas is less than solar, greater than $0.1 Z_\odot$, and consistent with that of the HII regions (0.20 to $0.25 Z_\odot$).

4.2. Metallicity of the Hot Outflow

To identify the major spectral components, we assumed a metallicity of $0.25 Z_{\odot}$, consistent with the HII region oxygen abundance, for the thermal plasma. Using the integrated spectrum, we investigate the best fitting abundance and the abundance ratios. Our model for the integrated count distribution includes the following components: (1) a foreground Galactic column with solar abundances and $N_H = 2.1 \times 10^{21} \text{ cm}^{-2}$; (2) a power law component with an intrinsic absorption component of $1.5 \times 10^{21} \text{ cm}^{-2}$, photon index $\Gamma = 2.47$, and normalization $9.20 \times 10^{-5} \text{ ph keV}^{-1} \text{ cm}^{-2} \text{ s}^{-1}$ at 1 keV; (3) an absorbed thermal component described by a *MEKAL* model with variable abundances; and (4) a hotter, absorbed thermal component with variable abundances. The abundances of Mg, Ne, Si, and Ca, relative to their solar values, are tied to the O abundance ratio; and we refer to this set of elements as the *alpha elements*, or Z_{α} . Aside from He, which is left fixed at solar abundance, all the other elements are varied with the Fe abundance, hereafter Z_{Fe} .⁹

For alpha element abundances from $Z_{\alpha} = 0.1 Z_{\odot}$ to $100 Z_{\odot}$, we fitted the temperature, absorbing column, and normalization of the two thermal components. The fit statistics in Table 5 show that the best fit is obtained for $Z_{\alpha} = 1.0 Z_{\odot}$. The fit is poor if $Z_{\alpha} \leq 0.25 Z_{\odot}$, but abundances higher than solar cannot be excluded. Higher metallicities are simply compensated by lower emission measures in the spectral fitting. Figure 16 illustrates the degeneracy using a model of the integrated spectrum. At temperatures of 0.3 and 0.7 keV, the spectrum is completely dominated by emission lines which are largely blended together at ~ 100 eV resolution. The strength of the Fe lines relative to the NeIX, NeX, MgXI, and SiXIII lines largely determines the shape of the count distribution. The spectrum looks almost the same when the continuum (i.e., normalization) is suppressed and the line emission (i.e., metallicity) is increased. The exception is at very low metallicity. The continuum of the $Z_{\alpha} = 0.25 Z_{\odot}$ model in Figure 17, for example, cannot be fit between 0.5 keV and 1.2 keV. Hence, we rule out metallicities lower than $0.25 Z_{\odot}$ for the thermal emission component. A practical upper limit can be placed on the wind metallicity when the minimum wind mass is considered (see §5.2.1).

The ratio Z_{α}/Z_{Fe} , in contrast, is well constrained. Figure 18 illustrates the distinct contribution of the alpha element emission lines and the iron emission lines to the spectrum.

⁹The solar abundance ratios in XSPEC 10.0 are photospheric values from Anders & Grevesse (1989). This meteoritic scale from Anders & Grevesse (1989) has significantly lower iron abundance. This controversy does not affect our analysis since we work in ratios relative to solar and define solar consistently throughout. We define solar abundances by the meteoritic values tabulated by Anders & Grevesse (1989). The solar values are still undergoing significant revision (e.g., Grevesse et al. 1996; Prieto et al. 2001).

We can set the alpha element abundances at just about any level, and a fit is found with an iron abundance (relative to solar) less than half the alpha element abundance. For example, the best fitting model, $Z_\alpha = 1.0 Z_\odot$, required $Z_{Fe} = 0.37 Z_\odot$; but Z_{Fe} increases to $43 Z_\odot$ when Z_α is set to $100 Z_\odot$. Figure 19 shows the 68%, 90%, and 99% confidence contours in the Z_{Fe} versus Z_α plane. The measured value of Z_α/Z_{Fe} clearly lies between 2.5 and 4.8 $Z_{\alpha,\odot}/Z_{Fe,\odot}$. Normalizing to the meteortic AG89 solar abundances decreases this ratio by 0.086 dex to Z_α/Z_{Fe} between 2.1 and 3.9.

In principle, the alpha element to iron abundance ratio constrains the origin of the metals. To illustrate the argument, we adopt the $0.1 Z_\odot$ series A models of Woosely & Weaver (1995). The IMF-averaged supernova ejecta have an O abundance $8 Z_{O,\odot}$ and an Fe abundance of $0.2 Z_{Fe,\odot}$. If the ejecta are mixed with interstellar gas of average metallicity $0.2 Z_\odot$, then the range of mass-loading factors, $\chi \equiv M_x/M_{ej} - 1$, implied by the measured alpha element enrichment is $\chi = 12$ to 36 . These values should not be taken as exact limits because yield calculations for Type II supernovae differ by up to a factor of three (e.g., Gibson, Loewenstein, & Mushotzky 1997 and references therein). The measured ratio of Z_α/Z_{Fe} in the outflow is supersolar but much lower than the ratio predicted for pure supernova ejecta. We note that the alpha element to iron abundance ratios reported for halo stars are similar over a broad sub-solar metallicity range (c.f., Wheeler et al. 1989 Figures 2 and 3).

4.3. Limits on Other Hot Reservoirs of Metals

4.3.1. Temperature Range in the Wind

Attempts to measure temperature variations with scale height from the S1 through S5 spectra yielded no clear trend. The color X-ray image in Figure 8 shows why. The color variations are not radial as would be expected in a freely expanding wind which cools adiabatically. Furthermore, as noted above, it is not clear that the red and green regions in the halo actually have significantly different temperatures. The red regions are less absorbed and appear to have a broader temperature range, but the number of photons is not high enough to describe the temperature range accurately.

The lines identified in the spectrum are consistent with the ionization balance expected in collisional ionization equilibrium for the fitted temperatures of the thermal components, 0.3 and 0.7 keV. Both components contribute to most of the lines. As can be seen in Figure 16, the exception is OVII, which is produced almost entirely by the 0.3 keV component. MgXII and SiXIV are present as a minority species in the hotter component alone, but their

lines are too weak to detect. Indeed the absence of these lines in the integrated spectrum, see Figure 10, is the strongest constraint on the emission measure of gas significantly hotter than 0.7 keV. Higher temperature gas would require an extremely low emission measure to avoid detection via these lines. Cooler gas, on the other hand, is plausibly (likely) present; but the high Galactic HI column in the direction of NGC 1569 combined with the uncertainties in the Chandra calibration at low energy prevent us from establishing any useful constraint on the cooler gas.

Strickland et al. (2000) have emphasized that the hottest component of the outflow may be very difficult to detect. We place upper limits on the normalization of components at 1.82 keV and 4.56 keV of 1.36×10^{-5} cm $^{-5}$ and 1.51×10^{-5} cm $^{-5}$ respectively. (These are 68% confidence limits.) Hence the surface brightness of a hotter component is down by a factor of at least 100 relative to the 0.3 keV and 0.7 keV components.

5. Discussion

The chemical and dynamical evolution of the wind are coupled because the supernova explosions that power the galactic outflow also enrich it with metals. Hydrodynamical models suggest that most of the material carried by a galactic wind is entrained interstellar gas rather than pure supernova ejecta (e.g., Suchkov et al 1996). This mass loading provides a second coupling between the dynamical and chemical evolution of the galactic wind since it reduces the temperature of the hot, supernova-driven wind while diluting the wind metallicity. By requiring the dynamical and chemical models to be self-consistent, we can constrain the properties of the outflow much better than was possible previously. The results allow us to discuss the role of the wind in the chemical evolution of the galaxy.

5.1. Wind Dynamics

5.1.1. The Existing Picture

The bipolar outflow in NGC 1569 was first recognized in H α images (Hodge 1974; de-Vaucoulers et al. 1974). Studies of the stellar population and radio continuum concluded the starburst was 10-20 Myr old (Israel ; O’Connell; Hunter et al. 1993) consistent with the measured dynamical age of the outflow (Heckman et al. 1995; Martin 1998). The mechanical energy produced, see Table 6, is equivalent to 3000 to 26,000 supernova explosions depending on whether the full starburst population or just the two super star clusters are considered. In either scenario, the implied rate of energy injection exceeds that required to generate a

superbubble which breaks out of the disk supersonically (e.g., Martin 1998).

The exact power requirement of the outflow in NGC 1569 is sensitive to the assumed distribution of disk and halo gas. For an average ambient density n_0 , the total mechanical energy needed to reproduce the observed sizes and expansion speeds of the shells is $\sim 2.8 \times 10^{55} (n_0/0.1 \text{ cm}^{-3})$ erg, where we have added the shells identified in Martin (1998). Comparison to Table 6 shows that the SSC's alone do not supply enough energy to drive the outflow. The Chandra images support the conclusion that the full starburst population powers the outflow because the wind appears to emanate from the entire stellar disk not just the central 100 pc.

Similarly, the Chandra results are consistent with the previous conclusion that the hot wind is not gravitationally bound to the galaxy (Heckman et al. 1995; Martin 1999). (Note, that in contrast, the warm shell is marginally bound to the dark halo.) The halo temperature fitted to ROSAT and ASCA data was shown to exceed the specific thermal energy needed to escape from the halo (Martin 1999, Figure 3), and the same is true of the revised thermal components at 0.3 keV and 0.7 keV. The hot wind will therefore escape unless mass loading accelerates the cooling by a large factor and/or the wind does a great deal of work against a putative gaseous halo. Since the combined luminosity of the two thermal components in our model, $L_x(0.3 - 6 \text{ keV}) = 8.18 \times 10^{38} \text{ ergs s}^{-1}$, is only a few percent of the average rate of mechanical energy injection, the radiative losses from the hot bubble are likely small. We discuss below whether the surprisingly complex spectrum and spatial distribution of the X-ray halo emission provide indirect evidence for the existence of such a halo via the interaction of the outflow with it.

The mass of the hot wind depends on the fitted emission measure and the assumed volume filling factor. Our results also confirm that the X-ray emission comes from the region interior to the H α -emitting shells as previous ROSAT imaging indicated (Heckman et al. 1995; Della Ceca et al. 1996). This result supports the assumption that the volume filling factor of the hot wind is of order unity, $f \sim 1$. If the hot wind and warm shell have similar pressure, then the volume filling factor of the warm gas must be $\epsilon \approx 0.01$ (Martin 1999). For these parameters, the implied mass loss rate in the hot wind is a few tenths of a solar mass per year, which is similar to the star formation rate (Martin 1999). We re-examine the mass carried by the wind, however, in light of its dependence on the wind metallicity which we have constrained for the first time. We find the rough scaling between mass flux in the wind and star formation rate still holds for a solar metallicity wind.

5.1.2. Revised Mass of X-Ray Emitting Nebula and Mass Loading

In § 4.2, we associated the 0.7 keV and 0.3 keV spectral components with the thermal emission from the outflow in the disk and halo, respectively. The fitted emission measures of these thermal components vary inversely with the wind metallicity. For a given emission measure, the mass of emitting gas follows directly from the volume of the emission region and the volume filling factor, f , of X-ray emitting gas. Figure 20 illustrates the inferred wind mass for various values of the alpha element abundance. The points correspond to the spectral models of Table 5.¹⁰ The spectral fitting constrains the alpha element abundance to be greater than 0.25 solar and the wind mass less than $6.2 \times 10^6 M_\odot$.

The spectral fitting allows alpha element abundances higher than solar, and those solutions imply a lower mass of hot gas. We use the mass of stellar ejecta to place a generous lower limit on the wind mass. From Table 6, the mass of stellar ejecta is $M_{ej} = 9.8 \times 10^4 M_\odot$ (10 Myr) to $3.8 \times 10^5 M_\odot$ (20 Myr).

For the best fitting model, $Z_\alpha = 1.0 Z_\odot$, the inferred mass of the X-ray halo is $2.80 \times 10^6 f^{0.5} M_\odot$. The disk holds nearly as much hot gas, roughly $7.34 \times 10^5 f^{0.5} M_\odot$. The total mass of hot gas is then $3.53 \times 10^6 f^{0.5} M_\odot$. For the continuous star formation model, the mass loading, $\chi \equiv (M_X - M_{ej})/M_{ej}$, is $\chi = 35$ to 8 for the age range 10 to 20 Myr. Figure 20 shows how much the inferred wind mass decreases for higher values of the alpha element abundance. For example, if the wind contains equal masses of stellar ejecta and entrained gas, i.e., $\chi = 1.0$, then $M_X = 7.6 \times 10^5 M_\odot$, and the alpha elements in the wind would be enriched to 40 times solar. Numerical simulations of the M82 superwind require a similar mass loading factor, ~ 5 , to reproduce the X-ray emission from that wind. These mass loading factors are within the range suggested by numerical simulations of winds (e.g., Suchkov et al. 1996).

5.1.3. Dynamical Evidence for a Gaseous Halo?

In § 4.3 we suggested that the spatial correlation between the hardest X-ray emission in the halo and the brightest regions of the halo might indicate a halo shock. In the absence of a gaseous halo, the wind would expand freely into the intergalactic medium, cooling adiabatically, after breaking through the gaseous disk. The high X-ray surface brightness

¹⁰To convert emission measure to mass, we assume cylindrical volumes for both the disk and halo components. The radius of each was taken as 1 kpc. The halo is assumed to extend to 1 kpc and the disk to 0.20 kpc. A filling factor of unity, $f \sim 1$, is shown.

and absence of a radial temperature gradient are inconsistent with this scenario. To generate a strong wind – halo interaction, the halo must be important dynamically. This criterion is certainly met if the swept-up mass of halo gas is comparable to the wind mass. For the minimum wind mass (which is 9 times smaller than our best estimate), this condition requires a halo density $n_h \geq 2.5 \times 10^{-3} (M_{ej}/3.8 \times 10^5) \text{ cm}^{-3}$. The implied column density could have eluded direct detection in the HI maps of Roberts (1968) and Stil & Israel (1998) but might be reachable by the ultra-deep observations of Mühle et al. (2001).

In a scenario where the wind generates a halo shock, the temperature of shocked halo gas would be directly related to the temperature of the wind emanating from the disk. Suppose we associate the hot, 0.7 keV, thermal component with this wind generation region. Then the wind emerges from the disk at roughly the sound speed, 430 km s^{-1} , and accelerates toward a terminal velocity $\sim \sqrt{3}c_s \sim 740 \text{ km s}^{-1}$ at large distances. The measured temperature of the *green* regions, 0.3 keV, corresponds to the temperature just behind a 550 km s^{-1} adiabatic shock. It appears at least plausible then, that expansion of the hotter thermal component generates a shock which dominates the emission at 0.3 keV.

The conundrum is that the shock front seen in the optical emission lines indicates substantially lower expansion velocities. The optical line ratios indicate most of the warm halo gas is photoionized, but the ratios do become more shock-like far out in the halo (Martin 1998) and are consistent with shock speeds $\sim 100 \text{ km s}^{-1}$, consistent with the expansion velocity of the H α filaments (60 to 120 km s $^{-1}$ along the sightline). The expected postshock temperature, about $4.5 \times 10^5 \text{ K}$, is too low to produce emission in the Chandra band. Direct measurement of the kinematics of the hot outflow would determine whether it has significant bulk motion, and therefore whether the two shocks are distinct.

The observational implications of the X-ray limb-brightening are quite significant. The interaction of the wind with this halo boosts the X-ray luminosity of the halo. The total luminosity of the 0.3 keV component is $5.0 \times 10^{38} \text{ ergs s}^{-1}$, which is comparable to that in the 0.7 keV component, $3.2 \times 10^{38} \text{ ergs s}^{-1}$. The main effect is simply to make the wind brighter without requiring extreme mass loading. Since L_x is still much less than the energy injection rate L_W , the radiative losses are far too small to stall the wind. Hence we expect the wind to blow through the halo and reach the IGM.

Comparison to the grid of models described by Silich and Tenorio-Tagle (2001) indicates the wind is still strong enough to escape from the halo. For the continuous star formation burst model, we find $\langle L_w \rangle = 2.1 \times 10^{40} \text{ ergs s}^{-1}$ ($\langle L_w \rangle = 8.3 \times 10^{40} \text{ ergs s}^{-1}$) at an age of 10 Myr (20 Myr). It is not clear whether this halo is typical of dwarf galaxies. Tidal debris from the interaction with the NGC1569-HI cloud could be the source of some (most?) of the halo gas.

5.2. Chemical Evolution

One expects the stars which power the galactic outflow to also enrich it. Indeed, simulations suggest the wind removes the new metals very efficiently (MacLow & Ferrara 1999), but we can now examine the efficiency directly.

5.2.1. Wind Abundance and Mass Entrainment

The wind carries metals recently ejected by supernovae and metals entrained from the ambient ISM. Figure 21 shows the resulting oxygen abundance of the wind for various mixing ratios of supernovae ejecta and ISM.

The wind metallicity is the sum of metals from supernovae and the entrained ISM divided by the wind mass, M_x .

$$Z_\alpha = M_{ej}(Z_{\alpha,SN} + \chi Z_{\alpha,ISM})/M_x. \quad (1)$$

Using the definition of the mass loading factor χ ,

$$M_x/M_{ej} = 1 + \chi, \quad (2)$$

to re-write Equation 1 in a form independent of mass, we have

$$Z_\alpha = (Z_{\alpha,SN} + \chi Z_{\alpha,ISM})/(1 + \chi). \quad (3)$$

Similarly, the abundance ratio of alpha elements to iron in the wind will be,

$$Z_\alpha/Z_{Fe} = (Z_{\alpha,SN} + Z_{\alpha,ISM})/(Z_{Fe,SN} + Z_{Fe,ISM}) \quad (4)$$

The curves in Figure 21 simply illustrate these relations for various the degrees of mixing. The transition from ejecta-dominated metals to ISM-dominated metals shows up as an inflection in the curves. The IMF-averaged metallicity of supernova ejecta is ~ 8 times solar for oxygen and ~ 0.2 times solar for Fe (model A runs of Woosley & Weaver (1995) at $0.1 Z_\odot$). The oxygen and iron yields of massive stars are only known to an accuracy of a factor of two to three. We plot the models for three plausible values of the supernova metallicity.

Each curve can be parameterized by the mass of stellar ejecta. The spectral degeneracy between the wind metallicity and the emission measure gives a unique mass for the X-ray emitting wind at each point (recall Figure 20). At any point in Figure 21, the mass of ejecta then follows directly from the wind mass and mass-loading factor. The actual value of M_{ej} likely lies between the two values for the continuous star formation scenario in Table 6.

These points are marked. A starburst duration of 20 Myr gives the maximum mass of ejecta and the lower limit on the mass loading factor. The corresponding upper limit on the wind metallicity is $O/H \lesssim 2$ (O/H) $_{\odot}$. Hence, even though the spectral analysis cannot rule out a very high metallicity wind, we find it would require an extremely low mass loading factor. Given the measured wind mass (for high metallicity), the low mass loading factors require more supernova ejecta than the current burst is likely to have produced.

We conclude that self-consistent chemical and dynamical models for the wind require the mass loading factor to be ~ 9 . Since the metallicity of the supernova ejecta is about $8/0.2 = 40$ times larger than the ambient ISM in NGC 1569, the metals from the recent starburst dominate unless the mass loading factor exceeds 40. Most of the metals in the outflow come from the supernovae ejecta not the entrained ISM even though the ISM supplies the majority of the mass in the outflow. This result explains why the measured ratio of alpha elements to Fe is higher than solar. We regard the model predictions for the alpha to iron abundance ratio in the bottom panel of Figure 21 very tentatively owing to the large uncertainties in the relative yields. It is encouraging, however, that the mass loading factors required to match the measured Z_{α}/Z_{Fe} value, see the end of § 4.2.2, are so close to our best estimates.

5.2.2. Metals Produced by the Burst vs. Metals in Wind

The parameters of our best model for the integrated spectrum, $Z_{\alpha} = 1.0$ Z_{\odot} in Table 5, imply the hot wind carries 3.5×10^6 M_{\odot} of gas which includes 3.4×10^4 M_{\odot} of oxygen. Models for higher abundance winds are less massive, so the mass of ejected metals is better constrained than the wind metallicity. Inspection of Figure 20 suggests the mass of oxygen ejected in the hot wind scales, roughly, as $M_O \approx 3.4 \times 10^4 \sqrt{Z_{\alpha}/Z_{\odot,\alpha}}$ M_{\odot} . The oxygen mass held by the warm phase ISM is considerably lower. Although the total mass is similar, the metallicity is down by a factor ~ 5 . Our new measurement of the metallicity of the HI disk (~ 0.20 Z_{\odot}) strongly suggests the neutral gas disk holds the majority of the gas phase oxygen, about $1.6 \times 10^5 (M_{HI}/8.4 \times 10^7)$ M_{\odot} of oxygen.¹¹ This disk enrichment shows that the metals were recycled rather than ejected during some, presumably *quiescent*, periods of star formation.

¹¹Scaled to a distance $d=2.2$ Mpc, the HI measurements of Reakes imply $M_{HI} = 8.4 \times 10^7$ M_{\odot} , which is considerably lower than the single dish measurement of Roberts (1.6×10^8 M_{\odot}). However, deep interferometric observations suggest an even larger value $M_{HI} \sim 2.4 \times 10^8$ M_{\odot} (Mühle et al. 2001). We take the smaller measurement to be representative of the *disk* and associate the larger values with the very extended halo component.

It is interesting to compare the mass of oxygen carried by the wind to the mass produced by the starburst. Table 6 shows the mass of oxygen produced for two fiducial star formation scenarios. The oxygen production from the Woosley & Weaver (1995) models was integrated over the stellar IMF. The least massive Type II supernovae progenitors live ~ 40 Myr and have probably not yet exploded. Comparison of the 5th and 6th lines in the Table shows the correction for this time lag is small relative to variation in the yield among the supernova calculations (e.g., Gibson et al. and references therein). The instantaneous burst model for the super star clusters produces only about one-tenth of the actual mass of oxygen in the outflow. The yield of nearly the full starburst population is apparently required to explain the metal content of the wind. This result is consistent with the previous conclusion that the super star clusters alone cannot power the wind.

5.2.3. *Retention of Metals and Burst Duty Cycle*

Nearly all the oxygen produced by the current burst is required to enrich the wind, so a previous generation of stars must have produced the metals held by the HI disk. The galaxy presumably retained metals during periods when no galactic wind was generated. Hence, we refer to these earlier epochs, when the star formation rate was lower and metals were recycled, as periods of quiescent star formation. If we adopt $M_{HI} = 8.4 \times 10^7 M_{\odot}$ as the mass of disk gas that is enriched to $\sim 0.20 Z_{\odot}$, then the mass of oxygen in the wind is about one-fifth of that held by the HI disk. Hence, the mass of stars that formed in the quiescent mode must be five to ten times larger than the stellar mass formed by the current burst, where the larger value applies for $M_{HI} = 1.6 \times 10^8 M_{\odot}$. Extending the stellar IMF down to $0.1 M_{\odot}$, the mass of stars formed in the quiescent phase is $M_* \approx 4 - 8 \times 10^7 (\tau/20 \text{ Myr}) M_{\odot}$.

The mass of stars required to enrich the HI disk can also be estimated from the metallicity of the disk and the total gas content of the system. If little mass was ejected from the galaxy previously, then the amount of quiescent star formation required to enrich the HI disk to a metal fraction Z is

$$M_*(t) = (e^{Z/y} - 1) M_g(t), \quad (5)$$

assuming instantaneous recycling of the metals. For an oxygen abundance of 20% solar, the oxygen mass fraction is $Z = 0.0019$. Substituting the oxygen yield $y = 0.0061$, which is appropriate for a lower mass cutoff $0.1 M_{\odot}$ (Woosley & Weaver 1995), into Equation 4 yields $M_* = 0.36 M_g(t)$, or $M_* \approx 3 - 6 \times 10^7 M_{\odot}$. Since these values are similar to our first estimate, it seems unlikely that large amounts of gas have already been expelled from NGC 1569. However, both estimates are strictly lower limits on the stellar mass. The difference of the dynamical mass of the disk $3.3 \times 10^8 M_{\odot}$ (Israel 1988) and the gas mass

yields an upper limit on the stellar mass of $1.7 - 2.5 \times 10^8 M_\odot$.

Uncertainty about the initial gas mass of the galaxy and the current stellar mass prevents us from drawing definitive conclusions about the fraction of total metals ejected from the galaxy by starburst winds. For purposes of illustration, however, Figure 22 shows a simple model of the enrichment history. For a closed box model to be consistent with the observed ISM abundance, the stellar mass must be near our minimum values. It is quite possible, however, that the stellar mass and gas mass are roughly equal. In this case, Figure 22 demonstrates that 30% to 50% of the initial gas mass could have been blown away (or stripped from the galaxy).

6. Summary

Galactic winds influence the chemical evolution of galaxies and enrich the intergalactic medium. Establishing the efficiency of mass and metal ejection has required empirical calibration, however, due to the complexity of exchange processes between phases of the ISM and the sensitivity of blowout to the structure of the gas disk. The result that might not have been anticipated is that, when a galaxy undergoes a starburst, most of the metals expelled by Type II supernovae are ejected from the galaxy even though the bulk of the ISM remains intact. The metals remain in the hot phase on a timescale that is long compared to the blowout timescale of the wind. The abundance of alpha elements is high relative to iron which is consistent with a Type II supernova-driven wind.

Our main results are as follows.

1. We resolve the hard emission into a population of point sources. The resolved sources contribute 57% (77%) of the 1.1 – 6 keV (2 –6 kev) emission, and the correction for unresolved point sources is estimated to be no more than 18% of the flux from the resolved population. The majority of the sources are believed to be high-mass X-ray binaries due to their variability, their spectral hardness, and the paucity of compact radio sources in NGC 1569. A new X-ray bright supernova remnant, CXOU043054.1+645043, is reported in the disk of NGC 1569. The low number of SNRs with detectable radio or X-ray emission in NGC 1569 is consistent with at least half of the supernovae exploding in low density environments where they radiate inefficiently – consistent with the generation of a galactic wind (e.g., Chevalier & Fransson 2001).
2. In contrast to previous analyses (Della Ceca et al. 1996), we find significant X-ray absorption from the disk of NGC 1569. The resulting color gradient is seen unambiguously in the

spectral imaging. Including it in the spectral modeling allows a higher continuum normalization and stronger emission lines. Requiring the fitted photoelectric absorption from the disk to be consistent with the HI column implied by the 21-cm brightness temperature constrains the metal abundance of the ambient gas disk to be greater than $0.1 Z_{\odot}$ and less than $1 Z_{\odot}$ which allows a value equal to that of the HII regions. We conclude that the neutral disk holds a higher metal mass than the wind or HII regions.

3. We confirm the strong spatial correlation between the extended X-ray emission and the $H\alpha$ filaments and discover that the halo consists of two X-ray emission components. The brighter, 0.3 keV, component is associated with the halo shock generated by the outflow. This emission comes from the highest X-ray surface brightness regions of the halo which are found near the $H\alpha$ filaments. The X-ray emission is detected over the full extent of the $H\alpha$ nebula but not convincingly beyond these filaments. The X-ray emission may come from the mixing layers between the shock and the bubble interior rather than the actual shock front. In either scenario, however, the presence of the shock implies the wind encounters a gaseous halo that was previously unrecognized. The wind – halo interaction significantly boosts the X-ray luminosity of the galaxy. We argue that the wind in NGC 1569 is likely powerful enough to blow through this halo and escape the galactic potential. The faint emission component in the halo is likely the wind fluid itself and may fill much of the volume.
4. The wind metallicity must be greater than $0.25 Z_{\odot}$ in order to fit the strong Mg and O lines in the spectrum. The large residuals in these lines in otherwise degenerate models with low metal abundance could not be recognized in lower signal-to-noise data. The spectrum alone provides no constraint on the maximum metallicity of the wind owing to a degeneracy between models with continuum normalization and metallicity. We can already conclude, however, that the wind metallicity does not exceed $O/H \approx 2 (O/H)_{\odot}$. Otherwise, the continuum normalization is pushed below that generated by the starburst ejecta alone which is known to within a factor of a few from simple population synthesis. Such metals predict that the burst produced 34,000 to 44,000 M_{\odot} of oxygen in 10 – 20 Myr. The wind carries about 34,000 M_{\odot} of oxygen. Hence, we conclude that the hot wind transports most of the metals synthesized by the burst.
5. We find the ratio of alpha elements to Fe is higher than the solar ratio. Supernovae yields are only known to within a factor of few, but the measured alpha element to iron ratio is clearly higher than the solar ratio and is consistent with a significant alpha element contribution from Type II supernova ejecta. This result is at first surprising given that most of the mass in the wind is entrained from the surrounding ISM. (We estimate $\chi \sim 9$). However, since NGC 1569 is a dwarf galaxy, the mean metallicity of

the ISM is only $0.20 Z_{\odot}$, and the mass loading would have to be more than a factor of 40 before the entrained oxygen mass exceeded the oxygen mass in the SNe ejecta.

6. The mass of oxygen leaving the galaxy in the wind is about 10% to 17% of the oxygen that was recycled into the neutral gas disk. Periods with lower star formation rates, i.e., quiescent star formation, must have produced at least five times as many stars (and metals) as the current burst. The total stellar mass and the initial gas mass are poorly constrained, so our chemical evolution models allow quite a large range for the ejected (or stripped) mass fractions over cosmic time.

Our results demonstrate that starbursts in dwarf galaxies do pollute the intergalactic medium. The question of whether dwarf or giant galaxies dominate this enrichment remains open (De Young & Gallagher 1990). However, the enrichment from dwarfs is particularly interesting in light of the large numbers of dwarf galaxies expected in the early universe, the measured enrichment of the Lyman alpha forest at redshift 3 to 4 (e.g., Songailia & Cowie 1996), and the low metallicities of many nearby dwarfs (Vader 1986). A definitive measurement of a supersolar alpha-element to iron abundance ratio in the IGM would allow one to conclude that starburst winds, rather than winds generated during non-starburst periods (e.g., Efstathiou 2000) or tidal debris (e.g., Gnedin 1998), dominate the IGM enrichment.

We thank Deidre Hunter for the use of her HST F555 image and Eric Wilcots and Stephanie Mühle for previews of their VLA 21-cm neutral hydrogen maps. Cornelia Lang reduced the 20 cm VLA data, and Nicole Homeier assisted with the optical observations. We thank Kim Weaver for providing comments on a draft of the paper. This research made use of the NASA/IPAC Extragalactic Database (NED) which is operated by the Jet Propulsion Laboratory, California Institute of Technology, under contract with the National Aeronautics and Space Administration. C.L.M. thanks the Sherman Fairchild Foundation for financial support. This work could not have been completed without funding from Smithsonian Astrophysical Observatory Award No. GO0-1140A under NASA contract No. NAS8-39073.

REFERENCES

Allen, M. L., & Kronberg, P. P. 1998, *ApJ*, 502, 218
Anders, E. & Ebihara, M. 1982, *Geochim. Cosmochim. Acta*, 46, 2363
Anders, E. & Grevesse, N. 1989, *GeCoA*, 53, 197

Arnaud, K.A., 1996, Astronomical Data Analysis Software and Systems V, eds. Jacoby G. and Barnes J., p17, ASP Conf. Series volume 101

Arp, H., & Sandage, A. 1985, AJ, 90, 1163

Buote, D. A., Fabian, A. C. 1998, MNRAS, 296, 997

Buote, D. A., & Canizares, C. R. 1994, ApJ, 427, 86.

Burton, W. B. 1985, A&AS, 62, 365

Chevalier, R. & Clegg 1985, Nature,

Chevalier, R. & Fransson 2001, ApJ, 558, 27.

Dahlem, M., Weaver, K. A., Heckman, T. 1998, ApJS, 118, 401

deVaucouleurs, G., deVaucouleurs, A., & Pence, W. 1974, ApJ, 194, 119.

Della Ceca, R., Griffiths, R. E., Heckman, T. M., & MacKenty, J. W. 1996, ApJ, 469, 662

De Young, D. S., & Gallagher, J. S. III, ApJ, 356, 15

Efstathiou, G. 2000, MNRAS, 317, 697.

Fabbiano, G., Zezas, A., Murray, S. S., 2001, ApJ, 554, 1035

Gibson, B. K., Loewenstein, M., & Mushotzsky, R. F. 1997, MNRAS, 290, 623

Gonzalez-Delgado, R. M., Pérez, Enrique, Tenorio-Tagle, G., et al. 1994, ApJ, 437, 239

Gnedin, N. Y. 1998, MNRAS, 294, 407

Green D. A., 2000, “A Catalogue of Galactic Supernova Remnants (2000 August version)”, Mullard Radio Astronomy Observatory, Cavendish Laboratory, Cambridge, United Kingdom (available on the World-Wide-Web at <http://www.mrao.cam.ac.uk/surveys/snrs/>).

Grevesse, N., Noels, A., & Sauval, A.J. 1996, ASP Conf. Ser. 99, 117

Heckman, T. M., Lehnert, M. D., Strickland, D. K., Armus, L. 2000, ApJS, 129, 493.

Heckman, T. M., Dahlem, M., Lehnert, M. D., Fabbiano, G., Gilmore, D., & Waller, W. H. 1995, ApJ, 448, 98

Ho, L. & Filippenko, A. V. 1996, ApJ, 466, 83.

Hodge, P. W. 1974, ApJ, 191, L21

Hunter, D. et al. 1993, AJ, 106, 1797

Hunter, D. A., O’Connell, R. W., Gallagher, J. S., & Smecker-Hane, T. A. 2000, AJ, 120, 2383

Israel, F. P. 1988, A&A, 194, 24

Israel F.P., De Bruyn A.G., 1988, A&A, 198,109

Israel, F. P., & van Driel, W. 1990, A&A, 236, 323

Karachentsev, ID., Tikhonov, N. A., & Sazonova, L. N. 1994, AstL, 20, 84.

Kennicutt, R. C. 1989, ApJ, 344, 685

Kennicutt, R. C. 1998, ApJ, 498, 541

Kennicutt, R. C. 1998, Ann. Rev. A&A, 36, 189

Kobulnicky, H. A. & Skillman, E. D. 1997, ApJ, 489, 636

Krautter, J., Zickgraf, F.-J., Appenzeller, I., Thiering, I., Voges, W., Chavarria, C., Kneer, R., Mujica, R., Pakull, M. W., Serrano, A., & Ziegler, B. 1999, A&A, 350, 743

Liedahl, D. A., Osterheld, A. L., & Goldstein, W. H. 1995, ApJ438, L115

Leitherer, C. et al. 1999, ApJS, 123, 3

MacLow, M.-M., & Ferrara, A. 1999, ApJ, 513, 142

Martin, C. L. 1997, ApJ, 491, 561

Martin, C. L. & Kennicutt, R. C., Jr. 1997, ApJ, 483, 698

Martin, C. L. 1998, ApJ, 506, 222

Martin, C. L. 1999, ApJ, 513, 156

Morrison, R. & McCammon, D. 1983, ApJ, 270, 119.

Mühle, S., Hüttemeister, S., Klein, U., & Wilcots, E. M. 2001, astro-ph/0107483.

Mushotzsky, R. et al. 1996, ApJ, 466, 686.

O'Connell, R. W., Gallagher, J. S., & Hunter, D. A. 1994, ApJ, 433, 65

Pannuti, T. G., Duric, N., Lacey, C. M., Goss, W. M., Hoopes, C. G., Walterbos, R. A. M., & Magnor, M. A. 2000, ApJ, 544, 780

Pence, W. D., Snowden, S. L., & Mukai, K. 2001, ApJ, in press

Prieto, C. A., Lambert, D. L., & Asplund, M. 2001, ApJ, 556 L63

Prestwich, A. H., 2002, in X-rays at Sharp Focus: Chandra Science Symposium, ASP Conf. Ser. xx, eds. S. Vrtilek, E. M. Schlegel, L. Kuhi

Raymond & Smith 1977, ApJS, 35, 419

Reed, J. E., Hester, J. J., Fabian, A. C., Winkler, P. F. 1995, ApJ, 440, 706

Reynolds, R.J., Tufte, S.L., Haffner, L.M., Jaehnig, K., & Percival, J. W. 1998, PASP, 110, 14

Rosati, P., Tozzi, P., Beacon, R. et al. 2001, *ApJ*, in press

Shopbell, P. L., Buckalew, B. A., Dufour, R. J., Walter, D. K. 2000, *BAAS*, 197, 7418

Silich, S. & Tenorio-Tagle, G. 2001

Songaila, A. & Cowie, L. L. 1996, *AJ*, 112, 335.

Stil, J. M. & Israel, F. P. 1998, *A&A*, 337, 64

Strickland, D. K., Heckman, T. M., Weaver, K. A., Hoopes, C. G., & Dahlem, M. 2001, *ApJ*, in press

Strickland, D. K., Heckman, T. M., Weaver, K. A., Dahlem, M. 2000, *AJ*, 120, 2965

Suchkov, A. A., Berman, V.G., Heckman, T. M., & Balsara, D.S. 1996, *ApJ*, 463, 528.

Tanaka, Y., Inoue, H., Holt, S. S. 1994, *PSAJ*, 46, 37

Taylor, C. L., Httemeister, S., Klein, U., & Greve, A. 1999, *A&A*, 349, 424

Tennant, A. F., Wu, K., Ghosh, K. K., Kolodziejczak, J. J., & Swartz, D. A. 2001, *ApJ*, 549, 43

Tenorio-Tagle, G. 1996, *AJ*, 111, 1641

Tenorio-Tagle et al. 1999 *mn* 309, 332

Vader, J. P. 1986, *ApJ*, 305, 669

Weaver, K. A., Heckman, T. M., & Dahlem, M. 2000, *ApJ*, 534, 684

Weiler, K. W., & Sramek, R. A. 1988, *ARA&A*, 26, 295

Wheeler, J. C., Sneden, C., & Truran, J. W. 1989, *ARA&A*, 27, 279

Woosley, S. E. & Weaver, T. A. 1995, *ApJS*, 101, 181

Table 1. NGC 1569 X-ray Point Sources

ID (1)	CXO Designation (2)	RA 2000 (3)	Dec 2000 (4)	C_{tot} (5)	C_S (6)	C_M (7)	C_H (8)	R_{PSF} (9)	$S_{\nu}(3)$ (10)	err (11)	$S_{\nu}(20)$ (12)	err (13)	R mag (14)	err (15)	$\log(f_x/f_V)$ (16)	Type (17)
1	CXOU043023.0+644913	04 30 23.05	+64 49 13.9	16.4±5.0	1.5±1.6	1.9±1.9	15±4.7	0.97	<0.09	...	<0.12	...	>23.7	...	>1.27	AGN
2	CXOU043025.2+645035	04 30 25.22	+64 50 35.6	81.2±9.5	2.5±1.9	11.1±3.8	68.5±8.8	0.91	<0.09	...	<0.12	...	>23.7	...	>2.87	AGN
3	CXOU043027.1+644926	04 30 27.15	+64 49 26.1	16.9±5.2	2.1±1.9	4.1±2.8	11.5±4.3	1.39	<0.09	...	<0.12	...	17.39	0.01	-4.47	Star
4	CXOU043030.9+645205	04 30 30.91	+64 52 05.3	182.8±14.0	10.6±3.8	39.9±6.8	133.2±12	0.77	<0.09	...	0.15	0.03	21.28	0.07	1.46	AGN
5	CXOU043032.8+644735	04 30 32.83	+64 47 35.3	27.3±6.0	1.5±0.8	3.1±0.7	28.1±6	1.05	<0.09	...	<0.12	...	>23.7	...	>1.78	AGN
6	CXOU043034.3+644740	04 30 34.31	+64 47 40.4	392.5±20.4	21.9±5.2	79.2±9.3	292.4±17.7	1.01	<0.09	...	<0.12	...	21.42	0.08	2.35	AGN
7	CXOU043035.2+645222	04 30 35.22	+64 52 22.1	14.3±4.4	1.5±0.7	1.5±1.5	13.5±4.2	1.11	<0.09	...	<0.12	...	>23.7	...	>1.13	AGN
8	CXOU043036.5+644921	04 30 36.53	+64 49 21.4	13.2±4.1	0.5±0.5	2.2±1.9	11.5±3.8	1.42	<0.09	...	<0.12	...	>23.7	...	>1.05	AGN
9	CXOU043039.0+645012	04 30 39.03	+64 50 12.8	41.4±7.1	19.5±4.8	17.4±4.7	5.4±3.0	1.36	<0.09	...	<0.12	...	17.11	0.07	-3.84	Star
10	CXOU043039.5+645108	04 30 39.59	+64 51 08.5	14.4±4.4	1.5±1.5	0.9±1.5	12.9±4.1	1.29	<0.09	...	<0.12	...	21.4	0.13	-0.96	Star
11	CXOU043043.7+644943	04 30 43.79	+64 49 43.0	12±3.9	2.2±1.9	4.2±2.5	6.5±2.9	1.16	<0.09	...	<0.12	...	19.05	0.02	-3.3	Star
12	CXOU043044.2+644924	04 30 44.21	+64 49 24.9	9.3±3.7	1.2±1.5	7.2±3.1	1.8±1.9	1.22	<0.09	...	<0.12	...	16.62	0.06	-5.78	Star
13	CXOU043044.8+645247	04 30 44.86	+64 52 47.0	40.5±6.8	11.5±3.8	14.5±4.2	15.5±4.3	0.82	<0.09	...	<0.12	...	18.94	0.02	-2.18	Star
14	CXOU043046.9+645106	04 30 46.90	+64 51 06.8	27.5±7.8	0.7±2	8.2±5.0	19.5±6.1	1.94	<0.09	...	<0.12	...	19.7	0.6	-1.87	XRB
15	CXOU043047.5+645055	04 30 47.55	+64 50 55.6	34.0±8.9	1.8±2.4	8.8±5.6	26.4±7.6	1.16	<0.09	...	<0.12	...	>16.8	0.6	>-4.3	XRB
16	CXOU043048.1+645050	04 30 48.14	+64 50 50.5	1150.5±35	139±12.5	462.4±22.4	550.1±24.3	1.16	<0.09	...	<0.12	...	>16.8	0.6	>-0.7	XRB
17	CXOU043048.2+645046	04 30 48.25	+64 50 46.6	159.3±13.6	3.5±2.5	19.8±5.3	136.9±12.5	1.30	<0.09	...	<0.12	...	>16.8	0.6	>-2.7	XRB
18	CXOU043048.5+645049	04 30 48.57	+64 50 49.6	9.7±6.9	19.4±5.1	2.6±3.9	4.1±3.3	1.33	<0.09	...	<0.12	...	>16.8	0.6	>-5.5	XRB
19	CXOU043048.6+645058	04 30 48.61	+64 50 58.5	637.2±26.2	32.1±6.4	148.6±13.1	457.5±22.1	1.52	<0.09	>19.3	...	>0.9	Cluster
20	CXOU043048.9+644940	04 30 48.93	+64 49 40.1	10.9±3.8	2.3±1.9	8.3±3.3	1.1±1.5	1.27	<0.09	14.5	0.02	-7.56	Star
21	CXOU043049.5+645042	04 30 49.56	+64 50 42.6	1.9±4.1	0.8±2	2.9±2.6	4.0±3.0	1.75	<0.09	>16.8	0.6	>-7.2	XRB
22	CXOU043049.8+645055	04 30 49.85	+64 50 55.4	144.5±12.9	8.5±3.5	33.5±6.6	103.4±10.8	1.18	<0.09	>19.9	...	>-0.0	Cluster
23	CXOU043050.2+645056	04 30 50.23	+64 50 56.2	-4.6±4.9	1.6±1.6	1.8±3.1	6.2±3.8	1.29	<0.09	>16.8	0.6	>31.9	XRB
24	CXOU043051.3+645050	04 30 51.38	+64 50 50.9	5.9±4.9	2.1±1.9	2.2±3	4.4±3.7	1.56	<0.09	>16.8	0.6	>-6.0	XRB
25	CXOU043051.7+645101	04 30 51.70	+64 51 01.4	6.7±3.5	0.5±0.5	2.4±2.2	4.8±3	1.17	<0.09	>16.8	0.6	>-5.9	XRB
26	CXOU043052.3+645042	04 30 52.34	+64 50 42.3	11.9±4.7	2.9±2.2	1.4±2.6	8.4±3.7	1.54	<0.09	>16.8	0.6	>-5.3	XRB
27	CXOU043053.3+645044	04 30 53.39	+64 50 44.1	23.8±5.6	1.7±0.8	8.3±3.5	16.5±4.6	1.47	<0.09	>16.8	0.6	>-4.6	XRB
28	CXOU043054.1+645043	04 30 54.11	+64 50 43.1	24.9±5.7	1.5±0.8	12.9±4.2	13.0±4.1	1.53	0.69	0.1	5.6	0.10	>16.8	0.6	>-4.6	SNR?
29	CXOU043057.4+645048	04 30 57.41	+64 50 48.6	231.0±15.9	3.5±2.2	28.6±5.9	199.9±14.8	1.40	<0.09	...	<0.12	...	>16.8	0.6	>-2.4	XRB
30	CXOU043058.0+644910	04 30 58.04	+64 49 10.9	24.3±5.5	1.5±1.5	6.1±2.9	17.7±4.7	1.46	0.95	0.03	0.85	0.04	>23.7	...	>1.66	AGN
31	CXOU043058.3+644852	04 30 58.37	+64 48 52.3	55.6±8	10.8±3.8	26.6±5.7	19.0±4.8	1.47	<0.09	...	<0.12	...	19.54	0.08	-1.31	Star
32	CXOU043101.9+644818	04 31 01.92	+64 48 18.4	25.4±5.6	1.5±0.7	6.5±2.9	19.6±4.9	1.52	<0.09	...	<0.12	...	22.01	0.13	0.16	AGN
33	CXOU043105.1+645058	04 31 05.16	+64 50 58.2	9.2±3.8	1.5±0.9	1.0±1.5	9.7±3.6	1.90	<0.09	...	<0.12	...	21.43	0.02	-1.38	Star
34	CXOU043111.5+644947	04 31 11.52	+64 49 47.1	24.3±5.5	0.5±0.5	7.3±3.1	17.5±4.7	1.32	<0.09	...	<0.12	...	18.77	0.02	-2.85	Star
35	CXOU043113.2+645229	04 31 13.20	+64 52 29.5	402.1±20.6	31.2±6	98.5±10.4	273.3±17.0	0.79	0.28	0.04	0.70	0.04	21.6	0.10	2.54	Star
36	CXOU043113.5+645217	04 31 13.51	+64 52 17.3	35.9±6.6	1.5±1.5	3.5±2.2	31.9±6.2	1.01	<0.09	...	<0.12	...	>23.7	...	>2.05	AGN

Table 1—Continued

ID (1)	CXO Designation (2)	RA 2000 (3)	Dec 2000 (4)	C_{tot} (5)	C_S (6)	C_M (7)	C_H (8)	R_{PSF} (9)	$S_{\nu}(3)$ (10)	err (11)	$S_{\nu}(20)$ (12)	err (13)	R mag (14)	err (15)	$\log(f_x/f_V)$ (16)	Type (17)
37	CXOU043114.0+645107	04 31 14.02	+64 51 07.9	773.0 ± 28.4	286.4 ± 17.4	343.6 ± 19.1	143.9 ± 12.5	1.00	<0.09	...	<0.12	...	12.83	0.01	-4.83	Star
38	CXOU043114.5+645024	04 31 14.54	+64 50 24.5	57.3 ± 8.1	1.3 ± 1.5	5.5 ± 2.7	51.5 ± 7.7	1.13	<0.09	...	<0.12	...	>23.7	...	>2.52	AGN
39	CXOU043116.8+644950	04 31 16.85	+64 49 50.0	4497.5 ± 67.8	827.0 ± 29.3	2160.5 ± 47.0	1511.5 ± 39.5	1.04	<0.09	...	<0.12	...	12.77	0.01	-3.12	Star
40	CXOU043120.5+645122	04 31 20.51	+64 51 22.5	178.5 ± 13.9	10.5 ± 3.6	36.5 ± 6.5	132.5 ± 12.1	0.94	<0.09	...	<0.12	...	22.23	0.16	2.31	AGN
41	CXOU043121.1+645029	04 31 21.12	+64 50 29.4	25.0 ± 5.5	3.5 ± 2.2	18.5 ± 4.7	4.0 ± 2.5	0.90	<0.09	...	<0.12	...	20.26	0.06	-1.45	Star
42	CXOU043124.4+645115	04 31 24.47	+64 51 15.5	72.6 ± 9.2	4.1 ± 2.5	18.1 ± 4.7	51.3 ± 7.8	0.87	<0.09	...	<0.12	...	>23.7	...	>2.75	AGN
43	CXOU043124.3+645121	04 31 24.38	+64 51 21.2	18.8 ± 5.7	1.8 ± 0.9	2.0 ± 1.8	21.0 ± 5.5	0.78	<0.09	...	<0.12	...	21.26	0.07	-0.82	Star
44	CXOU043125.1+645154	04 31 25.16	+64 51 54.2	328.8 ± 18.7	3.0 ± 2.2	6.2 ± 2.9	320.5 ± 18.4	0.88	<0.09	...	<0.12	...	19.67	0.03	0.57	AGN
45	CXOU043129.5+645053	04 31 29.52	+64 50 53.3	130.2 ± 12.1	4.0 ± 2.8	17.2 ± 4.6	109.8 ± 11.1	1.29	<0.09	...	<0.12	...	20.91	0.05	0.78	AGN

References. — (1) Reference ID # for this paper; (2) Chandra X-Ray Observatory identifier ; (3) J2000 Right Ascension from ACIS broadband image; (4) J2000 Declination; (5) Background-subtracted X-ray counts for each source in the 85 ksec observation detected in 0.3-6 keV band and 1σ uncertainty from photon statistics; (6) Background-subtracted X-ray counts for each source in the 85 ksec observation detected in broadband 0.3-0.7 keV soft X-ray band; (7) Background-subtracted X-ray counts for each source in the 85 ksec observation detected in broadband 0.7-1.1 keV medium X-ray band; (8) Background-subtracted X-ray counts for each source in the 85 ksec observation detected in broadband 1.1-6 keV hard X-ray band; (9) Ratio of source size to PSF size; (10) Flux of radio counterpart, if any, in mJy at 3.6 cm. Nondetections are listed as 3σ upper limits ; (11) 1σ uncertainty; (12) Flux of radio counterpart, if any, in mJy at 20 cm. Nondetections are listed as 3σ upper limits; (13) 1σ uncertainty; (14) R-band magnitude of optical counterpart, if any, from either our R-band imaging, or the HST F555W images from Hunter et al. (2000); (15) R-band 1σ uncertainty; (16) Log of the ratio of X-ray to optical flux, f_x/f_V : for this purpose we use $f_x(\text{erg s}^{-1}\text{cm}^{-2}) = 5.1 \times 10^{-18} x C_{tot}$ where C_{tot} is the number of detected photons from column 5 and $f_V(\text{erg s}^{-1}\text{cm}^{-2}) = 1.7 \times 10^{-9} \times 2.5^{-V}$ where V is approximated by the R magnitude from column 14. (17) Probable source type based on X-ray, radio, optical fluxes or IDs. Objects with $\log(f_x/f_V) < -0.5$ we tentatively identify as stars; Objects with $\log(f_x/f_V) < -0.5$ we tentatively identify as probable AGN. Objects in the disk of NGC 1569 without optical ID we identify as probable X-ray binaries.

Table 2. Fitted Models for Two Brightest Compact X-ray Sources in NGC 1569

Object	χ^2	$N(H)$ $\times 10^{22} \text{ cm}^{-2}$	Γ	kT (keV)	Z/Z_\odot	$F_a(0.3 - 6)$ $\text{erg cm}^{-2} \text{ s}^{-1}$	$F_u(0.3 - 6)$ $\text{erg cm}^{-2} \text{ s}^{-1}$	$L_u(0.3 - 6)$ erg s^{-1}
(1)	(2)	(3)	(4)	(4)	(6)	(7)	(8)	(9)
#16 Power Law	1.02	0.80 ± 0.19	3.66 ± 0.32	5.7×10^{-14}	47.7×10^{-14}	3.1×10^{38}
#16 MEKAL	0.87	0.15 ± 0.14	...	0.94 ± 0.14	0.03 ± 0.01	5.3×10^{-14}	13.7×10^{-14}	7.9×10^{37}
#16 Blackbody	1.46	0.0 ± 0.02	...	0.28 ± 0.02	...	4.4×10^{-14}	7.8×10^{-14}	4.5×10^{37}
#19 Power Law	0.91	0.72 ± 0.32	2.31 ± 0.45	5.0×10^{-14}	9.5×10^{-14}	5.4×10^{37}
#19 MEKAL	0.96	0.12 ± 0.08	...	2.99 ± 1.45	0.34 ± 0.41	3.9×10^{-14}	6.4×10^{-14}	3.6×10^{37}
#19 Blackbody	1.41	0.00 ± 0.38	...	0.42 ± 0.05	...	2.6×10^{-14}	3.5×10^{-14}	2.0×10^{37}

References. — (1) Model: All models include a foreground Galactic absorbing component with solar metallicity and $N(HI) = 2.0 \times 10^{21} \text{ cm}^{-2}$ and a foreground component with $0.25 Z_\odot$ to represent the ISM within NGC 1569.; (2) Reduced χ^2 ; (3) best fit $Z = 0.25 Z_\odot$ absorbing column density within NGC 1569 at 90% confidence ; (4) best fit power law photon index at 90% confidence ; (5) best fit temperature for MEKAL thermal plasma at 90% confidence ; (6) best fit metallicity for MEKAL thermal plasma at 90% confidence ; (7) Absorbed Model flux from 0.3–6 keV ; (8) Unabsorbed Model flux from 0.3–6 keV ; (9) Unabsorbed luminosity from 0.3–6 keV

Table 3: Models Fitted to Integrated Spectrum

model	N_H (cm^{-2})	kT (keV)	norm (cm^{-5})	N_H (cm^{-2})	kT, Gamma (keV, #)	norm (cm^{-5} , $\text{keV}^{-1}\text{cm}^{-2}$)	χ^2_ν	ν
wabs(vabs*M)	4.1×10^{21}	0.62	1.19×10^{-3}				3.12	160
DGHM96 wabs(M+M)	0	[0.63]	4.29×10^{-4}	0	[3.81]	3.30×10^{-4}	1.83	161
wabs(M+M)	0	0.66	4.53×10^{-4}	0	2.70	2.93×10^{-4}	1.72	159
DGHM96 wabs(M+P)	0	[0.64]	3.66×10^{-4}	0	[2.09]	1.13×10^{-4}	2.14	161
wabs(M+P)	0	0.67	4.65×10^{-4}	0	1.73	0.72×10^{-4}	1.79	159
wabs(vabs*M+vabs*M)	2.5×10^{21}	0.27	1.23×10^{-3}	1.1×10^{22}	0.73	1.41×10^{-3}	1.21	157
wabs(vabs*Pt+vabs*M+vabs*M)	3.9×10^{21}	0.25	1.55×10^{-3}	6.0×10^{21}	0.73	6.23×10^{-4}	1.20	157

Notes – The abundances are fixed at 0.25 Z_\odot . The [...] notation denotes a fixed parameter. The foreground absorption component has solar metallicity and a fixed column of $2.1\text{e}21 \text{ cm}^{-2}$. The models are MEKAL (M), power law (P), photoelectric absorption with solar abundance (wabs), and photoelectric absorption with 0.25 Z_\odot abundance (vabs). The power law fitted to the combined point sources (Pt) has $\Gamma = 2.40$, and $norm = 8.40 \times 10^{-5}$ photons $\text{keV}^{-1} \text{ cm}^{-2} \text{ s}^{-1}$ (at 1 kev) with an intrinsic (0.25 Z_\odot) absorbing component of $N_H = 2.1 \times 10^{21} \text{ cm}^{-2}$.

Table 4: Models Fitted to S1-5 Spectrum

model	N_H (cm^{-2})	kT (keV)	norm (cm^{-5})	kT (keV)	norm (cm^{-5})	N_H (cm^{-2})	kT (keV)	norm (cm^{-2})	chi2v	v
wabs(vabs*M+vabs*M) _{T1}	2.0×10^{17}	[0.61]	1.8×10^{22}	0	0	1.8×10^{22}	[0.61]	2.77×10^{-1}	1.57	129
wabs(vabs*M+vabs*M)	1.9×10^{21}	0.29	3.46×10^{-4}	0	0	6.7×10^{21}	0.73	2.63×10^{-4}	1.22	128
wabs(vabs*M+M+vabs*M)	3.9×10^{21}	0.28	6.70×10^{-4}	0.1	7.48×10^{-4}	8.22×10^{21}	0.73	2.59×10^{-4}	1.22	126
wabs(vabs*M+M+vabs*M)	8.1×10^{22}	0.10	41.69	0.34	1.47×10^{-4}	3.0×10^{21}	0.74	1.81×10^{-4}	1.17	127

Notes – The components are as described in the notes to Table 3. Point sources have been masked out, so their power law component is not included.

Table 5: Variable Abundance Models Fitted to Integrated Spectrum

Z_α (Z_\odot)	Z_{Fe} (Z_\odot)	χ^2_ν	$N_{H,1}$ (cm^{-2})	kT_1 (keV)	$norm_1$ (cm^{-5})	$N_{H,2}$ (cm^{-2})	kT_2 (keV)	$norm_2$ (cm^{-5})
0.10	0.12	1.364	4.38×10^{21}	0.22	1.00×10^{-2}	1.80×10^{21}	0.72	6.44×10^{-4}
0.25	0.14	1.246	2.98×10^{21}	0.31	2.19×10^{-3}	1.60×10^{21}	0.71	4.23×10^{-4}
0.50	0.21	1.195	3.09×10^{21}	0.31	1.36×10^{-3}	1.43×10^{21}	0.70	2.76×10^{-4}
1.00	0.37	1.185	3.0×10^{21}	0.31	6.40×10^{-4}	1.5×10^{21}	0.65	2.19×10^{-4}
5.00	1.41	1.194	5.5×10^{21}	0.25	2.81×10^{-4}	4.1×10^{20}	0.61	5.90×10^{-5}
10.0	4.26	1.200	3.2×10^{21}	0.31	9.51×10^{-5}	3.8×10^{21}	0.70	2.58×10^{-5}
100	43	1.197	3.8×10^{21}	0.25	1.10×10^{-5}	2.6×10^{21}	0.61	3.89×10^{-6}

Notes – All models contain a fixed Galactic absorption component ($1.2 \times 10^{21} \text{ cm}^{-2}$, 1.0 Z_\odot) and power law describing the point source component ($\Gamma = 2.40$, and $norm = 8.40 \times 10^{-5}$ photons $\text{keV}^{-1} \text{ cm}^{-2} \text{ s}^{-1}$ at 1 kev) with an intrinsic (0.25 Z_\odot) absorbing component of $N_H = 2.3 \times 10^{21} \text{ cm}^{-2}$. The alpha element abundance of the two thermal components is fixed at the 7 levels shown. The other elements are varied with iron as the temperatures and normalizations of the two thermal components are fitted. The intrinsic absorbing columns for each thermal component are varied independently and were assumed to solar abundance in this exercise.

Table 6: Power and Stellar Ejecta Supplied by Massive Stars

SFH ^a	C-SFR	C-SFR	I-Burst	I-Burst
Age	10 Myr	20 Myr	10 Myr	20 Myr
SFR ^a (M_{\odot} yr ⁻¹)	0.17	0.17
M_{*} ^b (1-100 M_{\odot})	1.7×10^6	3.4×10^6	3.1×10^5	3.1×10^5
M_{ejecta} ^b (M_{\odot})	9.8×10^4	3.8×10^5	4.5×10^4	8.7×10^4
E_W ^b (ergs)	6.8×10^{54}	2.6×10^{55}	3.1×10^{54}	6.9×10^{54}
$M_O(t)$ ^c (M_{\odot})	3.4×10^3	4.4×10^3
M_O (final) ^c (M_{\odot})	2.5×10^4	5.1×10^4	4.8×10^3	4.8×10^3

^a This table illustrates the mechanical, radiative, and chemical feedback in NGC 1569 for two star formation histories – an instantaneous burst (I-Burst) and a constant star formation rate (C-SFR). To illustrate the relative contribution of the two prominent super star clusters to the more widespread massive star population, we normalize the C-SFR model the the former using the total H α luminosity of the galaxy (Martin & Kennicutt 1997), but we normalize the I-Burst to the stellar mass of the two SSCs (Ho & Filippenko 1996).

^b Based on population synthesis models from Leitherer et al. (1999) which use a Salpeter IMF from 1 to 100 M_{\odot} and solar abundances. (Using 0.2 Z_{\odot} models makes negligible differences for our results.) The lifetime of the lowest mass Type II supernova progenitors is is 40 Myr in this model, so the instantaneous burst models reach their final yield, and the constant star formation rate model has not attained equilibrium rates. The value shown is the integral of the rate over 10 or 20 Myr as indicated.

^c We integrate the oxygen yields (Woosley & Weaver 1995) over the stellar intial mass function. We assume the least massive star that produces a Type II supernovae has an initial stellar mass of 10 M_{\odot} . Stars with initial masses larger than about 30 M_{\odot} have considerable reimplosion of heavy elements, and no star more massive than 40 M_{\odot} contributes to the yield in this model.

Fig. 1.— X-ray point sources and star clusters in the main stellar body of NGC 1569. The greyscale shows a logarithmic representation of the R-band optical image and the contours show the adaptively-smoothed Chandra ACIS broadband 0.3-6 keV image. Contour levels are drawn every factor of 4 at 0.0005, 0.0020, 0.0080, 0.032, 0.128, 0.5, 2.0, and 8.0 photons $\text{s}^{-1} \text{arcmin}^{-2}$.

Fig. 2.— HST F555W broadband optical image (logarithmic greyscale) with adaptively-smoothed X-ray image (contours) showing the central X-ray point sources and star clusters in the nucleus of NGC 1569. Contour levels are the same as Figure 1.

Fig. 3.— Two-color diagram for point sources. Lines represent the colors of model spectra. (Upper panel) Sources projected against the main body of NGC 1569. Power laws with photon indices of $\Gamma=1.5$, $\Gamma=2.5$, $\Gamma=3.5$, and a blackbody spectrum with a temperature $kT=0.2 \text{ keV}$ are shown for several foreground HI column densities. (Lower panel) Sources within a few arcminutes of the disk. MEKAL thermal plamsas with temperatures $kT=1.0$ and $kT=2.0 \text{ keV}$ are shown for several foreground HI column densities. Objects identified as probable stars in Table 1 on the basis of f_X/f_V are indicated.

Fig. 4.— Histogram of the hard-band (1.1–6 keV) source fluxes for 14 point sources in NGC 1569. The solid line shows a cumulative luminosity function with slope $\alpha = 0.5$ normalized to the highest luminosity bin (not a fit).

Fig. 5.— Contours of 0.3-6 keV X-ray emission on $\text{H}\alpha$ image. The contours are spaced by a factor of 1.347 from 0.00594 to 1.696 cnts s^{-1} per square arcminute. The $\text{H}\alpha$ image is displayed on logarithmic scale, and the filaments identified by Hunter et al. (1993) are marked. White bar represents 1'.0.

Fig. 6.— X-ray contours on $\text{H}\alpha$. Letters mark regions of maximal expansion velocity in the $\text{H}\alpha$ nebula from Martin (1998). Note that the fingers of X-ray emission protrude into these shells. Apertures discussed in the paper are marked in green. Circle marks the position of SSC A. The length of the rectangular apertures is 1 kpc.

Fig. 7.— Composite 3-color image of NGC 1569 with the Chandra 0.3-6 keV X-ray emission in green, $\text{H}\alpha$ emission in red, and optical 6450Å continuum in blue. Contours show the 21-cm neutral hydrogen column density at levels of $1 \times 10^{21} \text{ cm}^{-2}$ (bold), $4 \times 10^{21} \text{ cm}^{-2}$ (solid line), and $7 \times 10^{21} \text{ cm}^{-2}$ (dashed line).

Fig. 8.— Chandra true-color X-ray image of NGC 1569. Red, green, and blue represent the soft (0.3 - 0.7 keV), medium (0.7 - 1.1 keV), and hard (1.1 - 6 keV) regions of the Chandra bandpass. The images have been adaptively smoothed (see text). Contours are the same as in Figure 7.

Fig. 9.— Contours of soft color $C_1 = (M - S)/(M + S)$ on broadband X-ray intensity. The softest regions, $C_1 \approx 0.3$ to 0.5, correspond to the faintest regions of the halo.

Fig. 10.— Integrated spectrum of NGC 1569. The contribution of resolved point sources is shown in blue. The red line shows the spectrum of the diffuse component. Prominent lines of O, Ne, Mg, and Si are marked. The Fe L lines are largely blended, so we have marked only the energies of the strongest line from each ionization state FeXVII through FeXXIV. The blue line represents the background simulated from a set of deep exposures (see § 2.1.1). The OVII and OVIII lines are prominent whichever mode of background-subtraction is employed, but some of the features near Si lines may be residuals of the background subtraction.

Fig. 11.— Integrated spectrum of NGC 1569. The folded spectrum and residuals are shown for several models from Table 3. See discussion in the text.

Fig. 12.— Count distributions of the *red* and *green* regions of the southern halo (cf. Figure 8). The physical parameters of the emitting plasma are dicussed in § 3.2.2 and § 3.3.3.

Fig. 13.— Geometry of the disk and outflow.

Fig. 14.— Comparison of the diffuse emission spectrum on the south and north side of the disk. Spectra from different apertures are offset for ease of comparision, and the northern spectra have been scaled to match the 1 to 2 keV counts in the southern spectra.

Fig. 15.— Equivalent hydrogen absorption column, fitted to the thermal emission model, versus projected distance from the plane of the disk. The total column includes absorption from the disk of NGC 1569 and foreground Galactic absorption. The results are shown for three hypothetical values of the gas-phase metallicity in NGC 1569. The foreground column is assumed to have solar metallicity. The thick, solid line represents the total Galactic and NGC 1569 hydrogen columns measured from 21-cm emission. The error bars represent the 90% confidence range for the assumed two component model. We assume solar abundances (Anders & Ebihara 1982) for the foreground, Galactic gas but vary the metallicity of the intrinsic absorbing column of the NGC 1569 disk.

Fig. 16.— The tradeoff between metallicity and normalization of the thermal components in our models of the integrated spectrum. The blue, green, and red lines illustrate the hard thermal, soft thermal, and power law components for two different models from Table 5 – the $1.0Z_{\alpha,\odot}$ model in panel a and the $100Z_{\alpha,\odot}$ model in panel b. The spectra resulting from these two models are difficult to distinguish.

Fig. 17.— Fits to the integrated spectrum (points) with variable abundances. Folded spectra and residuals illustrate three models from Table 5: $Z_{\alpha} = 100 Z_{\alpha,\odot}$ (black), $1.0 Z_{\alpha,\odot}$ (blue), and $0.1 Z_{\alpha,\odot}$ (magenta). The spectral normalizations vary a great among these models as illustrated in Table 5.

Fig. 18.— Relative contribution of alpha elements and iron to the spectral model $wabs(vabs^*Pt + vabs^*M + vabs^*M)$. The $Z_\alpha = 1.0Z_{\alpha,\odot}$ from Table 5 is compared to models with little iron ($0.1Z_{Fe,\odot}$) (red) and a model with a paucity of alpha elements ($0.04Z_{\alpha,\odot}$) (green). (a) Prominent lines are labeled for the models. (b) Changing the ratio of alpha elements to iron has a measurable effect on the folded spectrum.

Fig. 19.— Elemental abundances fitted to the spectrum of the diffuse gas. The cross marks the best fit. Contours represent the 60%, 90%, and 99% confidence levels. The O/H and Fe/H abundance ratios are shown relative to the solar photospheric values of Anders & Grevesse (1989). On the more common solar meteoritic scale (Anders & Grevesse 1989), the relative Fe abundances are 0.085 dex higher. Note the Mg, Ne, Si, and Ca abundances are tied to O, and the other metals vary with the Fe abundance.

Fig. 20.— Implications of the spectral degeneracy between the fitted emission measure and metallicity of the diffuse hot gas. (Top) Dependence of the inferred gas mass on the assumed alpha element abundance (in solar units). (Bottom) The inferred mass of oxygen in the wind increases slowly as the alpha element abundance of the spectral model is increased, i.e. $M_O \propto Z_\alpha^{0.55}$.

Fig. 21.— Entraining interstellar gas in the hot supernova-driven wind affects the O abundance and the O/Fe abundance ratio in the wind. As the mass loading increases (toward the right), the O and O/Fe decrease toward their values in the ISM (see § 5.2.1). Three tracks are shown to illustrate the uncertainty in the supernova yields. Using the relation between $M_x - Z_\alpha$ from the fitted spectral models, the curves can be parameterized by the implied mass of stellar ejecta at each point. At a given metallicity (and therefore wind mass), a high mass loading factor implies a low mass of stellar ejecta in the wind. The solid circles delimit the mass of stellar ejecta produced by the starburst model after a time of 10 Myr ($9.8 \times 10^4 M_\odot$) and 20 Myr ($3.8 \times 10^5 M_\odot$). The Chandra measurements for O and O/Fe combined with the Starburst 99 estimate for the mass of supernova ejecta defines the data points and error bars. Consistent models require substantial mass loading of $\chi \sim 9$.

Fig. 22.— Model chemical enrichment history as a function of gas mass fraction. The solid line shows a closed box model assuming instantaneous recycling. The dashed lines show the evolutionary tracks if 75%, 50%, and 25% of the oxygen or an equivalent fraction of the gas mass is lost from the galaxy. The large symbol with error bars shows the *full permitted range* of observed gas mass fraction ($0.35 < \mu < 0.73$; see text) and ISM metallicity of NGC 1569 from HII regions ($0.2 < Z/Z_\odot < 0.25$).

This figure "cmartin_fig1.gif" is available in "gif" format from:

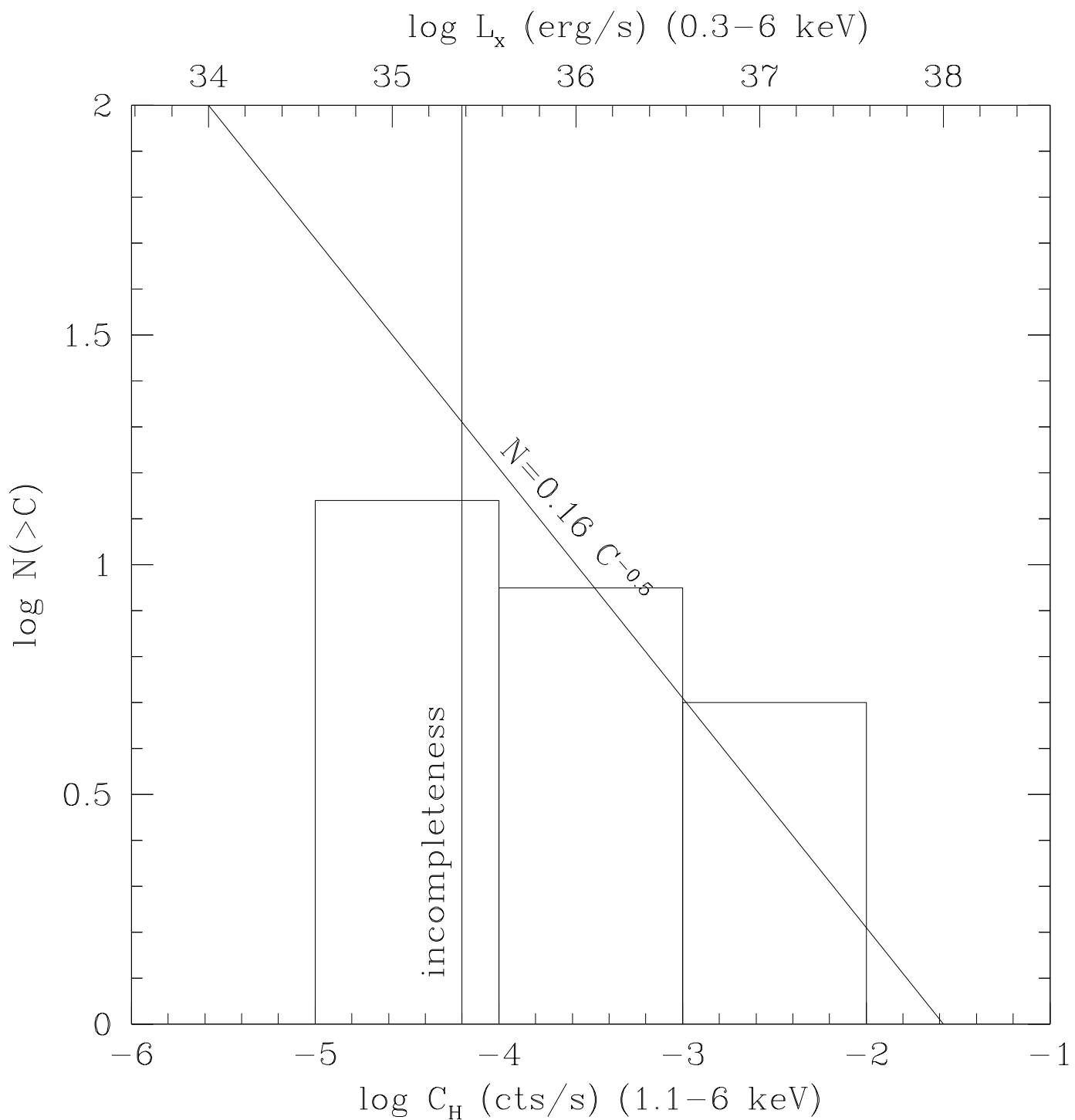
<http://arxiv.org/ps/astro-ph/0203513v1>

This figure "cmartin_fig2.gif" is available in "gif" format from:

<http://arxiv.org/ps/astro-ph/0203513v1>

This figure "cmartin_fig3.gif" is available in "gif" format from:

<http://arxiv.org/ps/astro-ph/0203513v1>



This figure "cmartin_fig5.gif" is available in "gif" format from:

<http://arxiv.org/ps/astro-ph/0203513v1>

This figure "cmartin_fig6.gif" is available in "gif" format from:

<http://arxiv.org/ps/astro-ph/0203513v1>

This figure "cmartin_fig7.gif" is available in "gif" format from:

<http://arxiv.org/ps/astro-ph/0203513v1>

This figure "cmartin_fig8.gif" is available in "gif" format from:

<http://arxiv.org/ps/astro-ph/0203513v1>

This figure "cmartin_fig9.gif" is available in "gif" format from:

<http://arxiv.org/ps/astro-ph/0203513v1>

This figure "cmartin_fig10.gif" is available in "gif" format from:

<http://arxiv.org/ps/astro-ph/0203513v1>

This figure "cmartin_fig11.gif" is available in "gif" format from:

<http://arxiv.org/ps/astro-ph/0203513v1>

This figure "cmartin_fig12.gif" is available in "gif" format from:

<http://arxiv.org/ps/astro-ph/0203513v1>

This figure "cmartin_fig13.gif" is available in "gif" format from:

<http://arxiv.org/ps/astro-ph/0203513v1>

This figure "cmartin_fig14.gif" is available in "gif" format from:

<http://arxiv.org/ps/astro-ph/0203513v1>

This figure "cmartin_fig15.gif" is available in "gif" format from:

<http://arxiv.org/ps/astro-ph/0203513v1>

This figure "cmartin_fig16a.gif" is available in "gif" format from:

<http://arxiv.org/ps/astro-ph/0203513v1>

This figure "cmartin_fig16b.gif" is available in "gif" format from:

<http://arxiv.org/ps/astro-ph/0203513v1>

This figure "cmartin_fig17.gif" is available in "gif" format from:

<http://arxiv.org/ps/astro-ph/0203513v1>

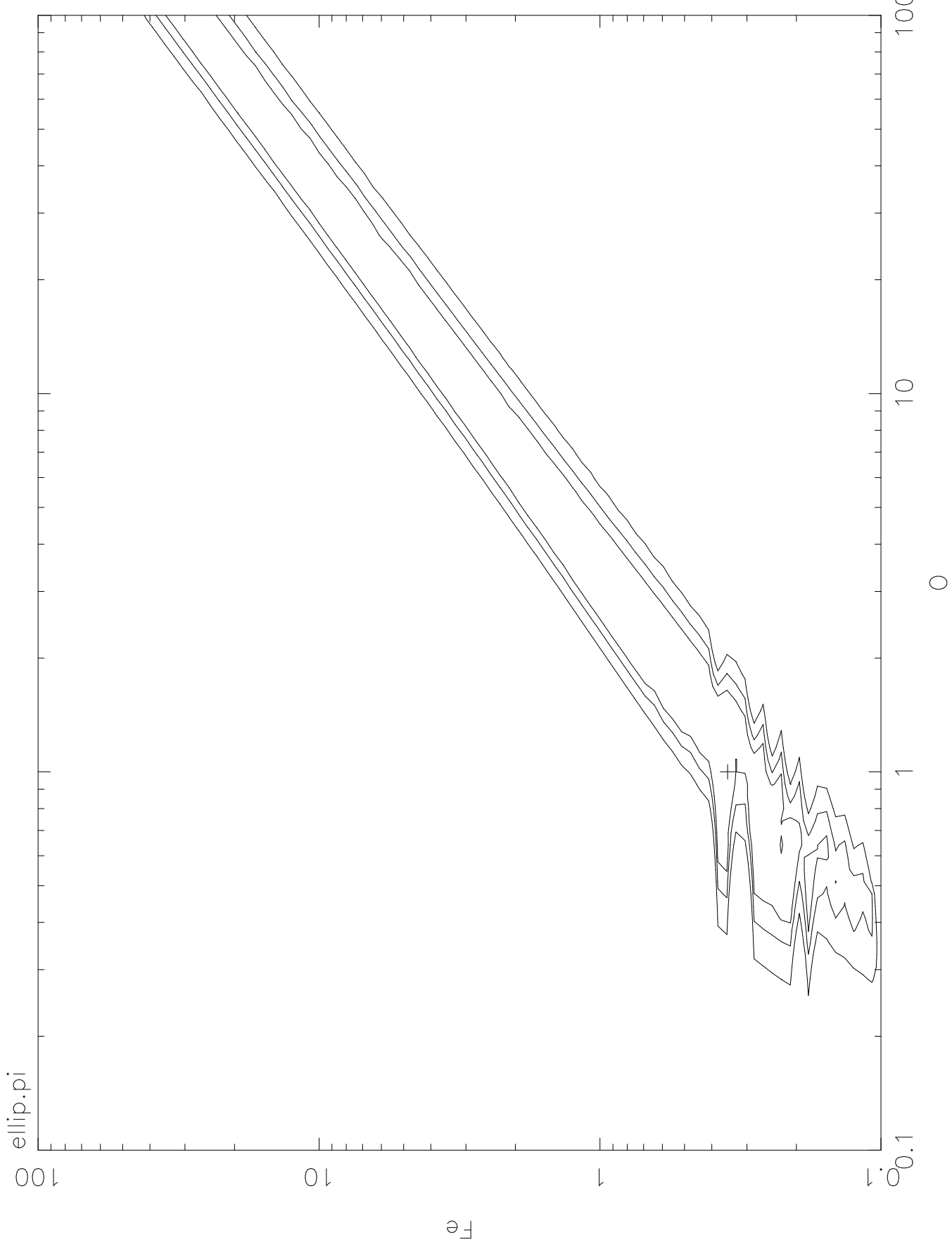
This figure "cmartin_fig18a.gif" is available in "gif" format from:

<http://arxiv.org/ps/astro-ph/0203513v1>

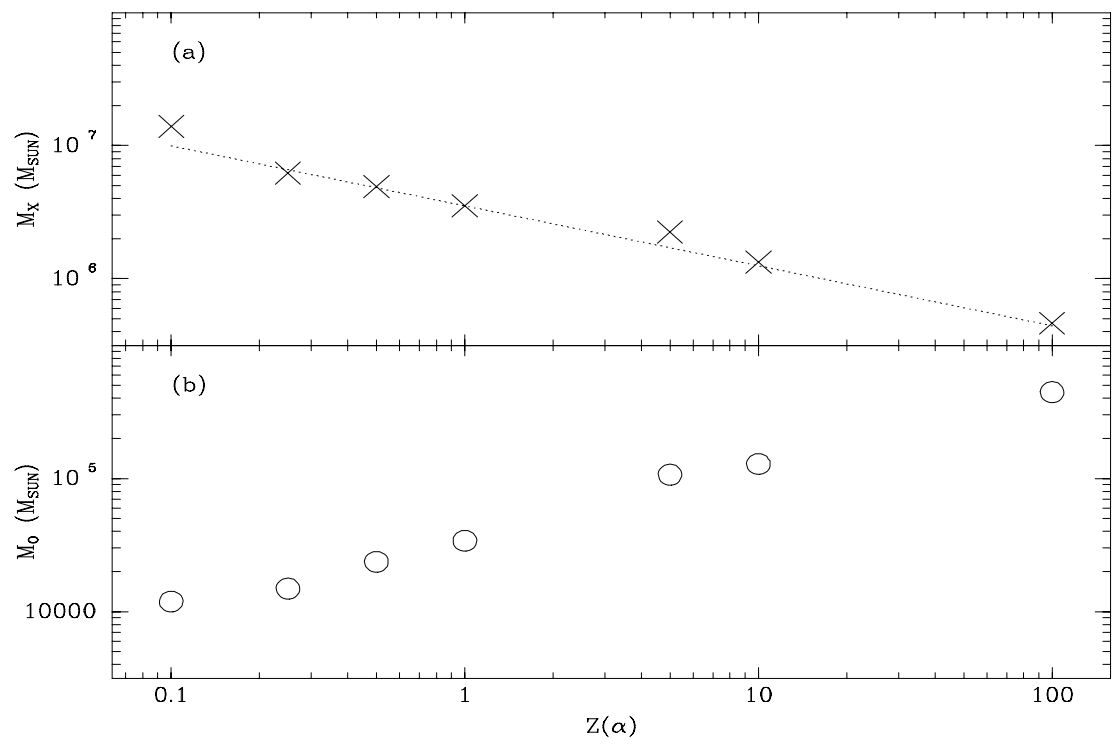
This figure "cmartin_fig18b.gif" is available in "gif" format from:

<http://arxiv.org/ps/astro-ph/0203513v1>

Confidence contours



20-Nov-2001 09:01



This figure "cmartin_fig21.gif" is available in "gif" format from:

<http://arxiv.org/ps/astro-ph/0203513v1>

